Technische Universität München
Fakultät für Physik

Graduation paper from the Bachelor of Science in Physics

Charged Pion Spectra in Pion-Nucleus Reactions at 1.7 GeV c^{-1}

Spektren geladener Pionen in Pion-Kern Reaktionen bei 1.7 GeV c^{-1}

Ulrike Sabine Fahrendholz
03660158

31th July 2017

Primary reviewer: Prof. Dr. L. Fabbietti
Supervisors: Steffen Maurus, Joana Wirth
Secondary reviewer: Prof. Dr. S. Bishop

Contents

1 Introduction

Long before the quark model has been developed, a theoretical description of a particle transfering the strong interaction between nucleons inside a nucleus was introduced by Yukawa.[1] These particles have been identified as pions. Besides the neutral pion, which consists of a mixture of two quark-antiquark pairs, ($\pi^0 = 1/\sqrt{2}(u\bar{d} + d\bar{u})$), the charged pions π^+=$u\bar{d}$ and $\pi^- = d\bar{u}$ can be found. Their mass is $m_{\pi^\pm} = 139.6\,\mathrm{MeV}$ and their lifetime is $\tau_{\pi^\pm} = 2.6 \cdot 10^{-8}$s.[8]
The present work will discuss charged pion production in π^-C collisions at beam momenta of 1.7 GeV / c at the HADES[1] experiment at GSI[2] Darmstadt.
While the pion production cross sections of photon induced reactions show a linear dependence on the mass number of the nucleons $\sigma \sim A$, protons have $\sigma \sim A^{0.8}$. For pA-reactions, secondary pions, which can further interact, are generated. Primary pions from the beam react mostly with the surface[3] of the nucleons, as their cross section for the reaction with nucleons is $\sigma \sim A^{2/3}$. This is reasoned by their short mean free path, which is $\lambda = 1.5\,\mathrm{fm}$ for the beam momentum of 1.7 GeV / c, in nuclear matter with particle dimensions of $d_C = 5.5\,\mathrm{fm}$ for Carbon.[14]
To investigate the π interaction with the nucleus, the production of K^0_S was measured by the FOPI[4] spectrometer, which observed $\pi^- A$ reactions at beam momenta of 1.15 GeV / c. Here, the cross sections for kaon production are dependent on the target material by $\sigma(K^0_S) \sim A^{2/3}$.[5]
One of the motivations for the HARP experiment was to make a systematic study of precise hadron production for πA reactions over a wide momentum and angle range[5] as a valuable validation of hadron production models. Double-differential charged pion-production cross sections $\mathrm{d}^2\sigma_{\pi^\pm}/\mathrm{d}p\mathrm{d}\Omega$ for pion-nucleus reactions were studied. The beam momenta were ranging from 3 GeV / c to 12.9 GeV / c. The employed targets were made

[1] **H**igh **A**cceptance **D**i-**E**lectron **S**pectrometer
[2] Gesellschaft fr Schwerionenforschung
[3] The dependence between the nucleus's radius R and the mass number A is $R \sim A^{1/3}$, thus the relation between the cross section for $\pi^- A$ and the radius is of the order of the surface: $\sigma \sim R^2$.
[4] The name FOPI originates from its full angular acceptance (4π)
[5] $100\,\mathrm{GeV/c} \leq p \leq 800\,\mathrm{GeV/c}$ and $0.35\,\mathrm{rad} \leq \theta \leq 2.15\,\mathrm{rad}$ or $20° \leq \theta \leq 123°$

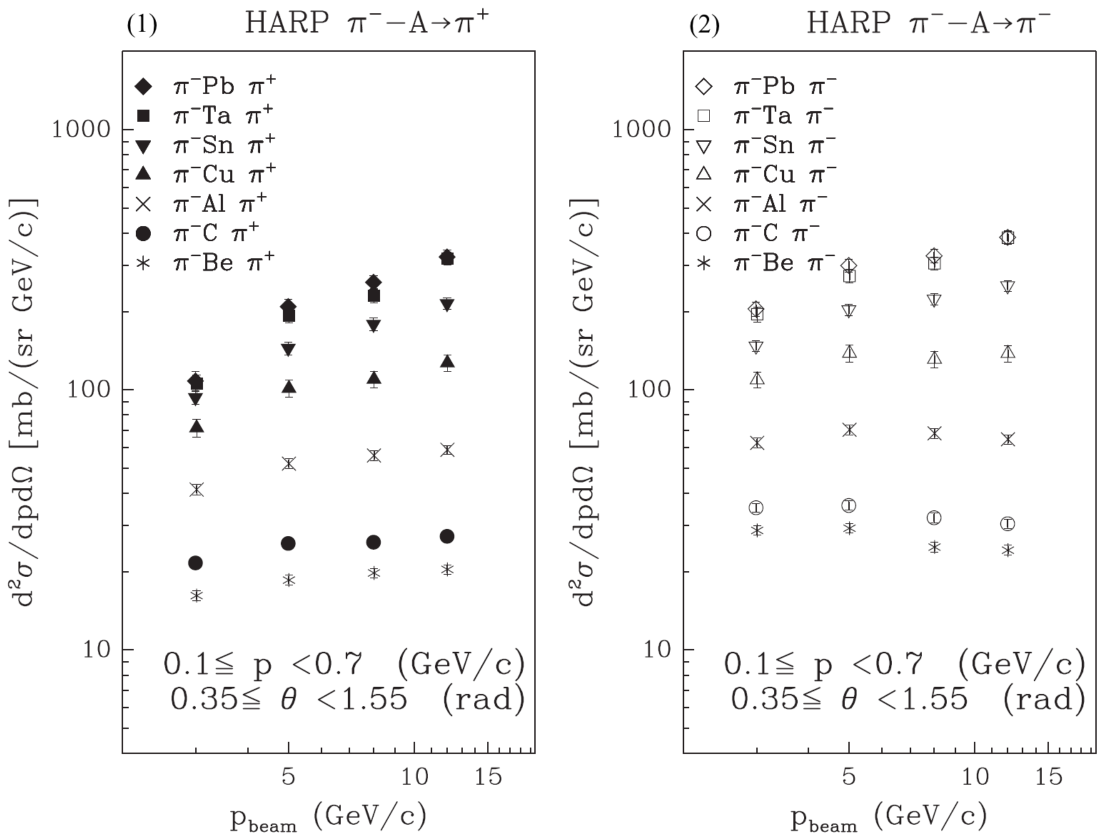

FIGURE 1.1: Dependence of $\mathrm{d}^2\sigma_{\pi^\pm}/\mathrm{d}p\mathrm{d}\Omega$ from the beam momentum p_{beam} for different target materials. (1) shows the double-differential cross-section $\mathrm{d}^2\sigma_{\pi^+}/\mathrm{d}p\mathrm{d}\Omega$ for the production of positive pions π^+ for different π^-A collisions, while (2) displays the cross-section $\mathrm{d}^2\sigma_{\pi^-}/\mathrm{d}p\mathrm{d}\Omega$ for negative pions π^- in the same reactions. [6]

of beryllium, aluminium, carbon, copper, tin, tantalum or lead, thus a large range of target atomic numbers was given.[6]
Figure 1.1 shows the cross sections $\mathrm{d}^2\sigma_{\pi^\pm}/\mathrm{d}p\mathrm{d}\Omega$ plotted over the different used beam momenta p_{beam} for the different target materials.

On the other hand, the dependence of $\mathrm{d}^2\sigma_{\pi^\pm}/\mathrm{d}p\mathrm{d}\Omega$ on the atomic mass number A has been plotted in Fig. 1.2. As depicted, the points follow a nearly linear curve. For pure surface interaction of the pions with the material the slope of the curve is of the order of 2/3.

New points could be added in the plots shown in Fig. 1.1. Two could be added to the carbon data for charged pion production.
Additionally, the plots from Fig. 1.2 could be completed by new points to see the dependence on the surface term for lower beam momenta than the ones used at HARP.

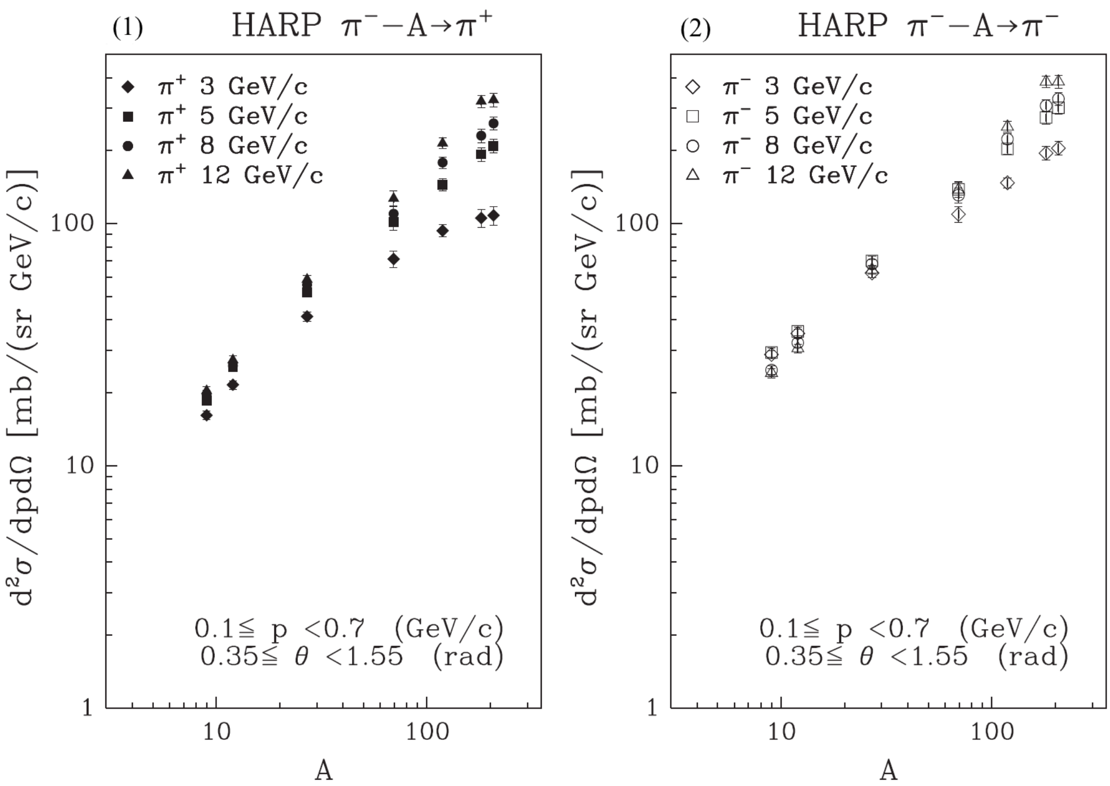

FIGURE 1.2: Dependence of $\mathrm{d}^2\sigma_{\pi^\pm}/\mathrm{d}p\mathrm{d}\Omega$ from the atomic mass number A of the targets for different beam momenta. (1) shows the production of positive pions, while (2) depicts the one for negative pions. [6]

This thesis is structured in the following way: After introducing the HADES experiment, the UrQMD and GiBUU transport models will be briefly presented. Afterwards, the analysis methods to obtain the pion spectra posed as results will be demonstrated.

2 HADES Experiment

The analysed $\pi^- C$ data was taken with the **H**igh **A**cceptance **D**i-**E**lectron **S**pectrometer (HADES) experiment at the GSI Helmholtzzentrum für Schwerionenforschung in Darmstadt, Germany. It is a fixed target experiment, providing proton-proton (pp), proton-nucleus (pA), nucleus-nucleus (AA), and pion-nucleus (πA) collisions. The beam particles are provided by SIS18, a 216 m circumference synchrotron, and are accelerated to energies of $1-2$ GeV per nucleon for heavy ions, up to 4.5 GeV for protons. Secondary pion-beams are available up to a maximal kinetic energy of about 2 GeV. [2][3]
HADES was initially developed to measure rare electromagnetic decays of the vector mesons, like ρ, ω and Φ. Electrons and positrons, which are the products of the electromagnetic decay, do not interact strongly and are therefore not distorted by the medium. Hence, the dielectron pairs carry information about the modified properties of the vector mesons inside of the nuclear matter, which can be measured and used to probe theoretical predictions. While the heavy-ion reactions form hadronic matter at two or three times higher nuclear matter densities and moderate temperature, pion or proton induced reactions with nuclei embed the vector mesons into normal nuclear matter.[3]

Figure 2.1 shows a schematic overview of the HADES detector assembly. The main features are the RICH[1] detector for hadron-electron discrimination, two sets of MDCs[2] in front and after the magnetic field as tracking system and the META[3] consisting of the RPC[4] and the TOF[5] detector as part of the time of flight measurement. Additionally, the pion tracker CERBEROS, the START system, which is used to observe beam properties and provides the start signal for the time of flight measurement, and the Pre-Shower detector for electromagnetic shower processes are shown in the figure. The spectrometer covers polar angles from $15° \leq \theta \leq 85°$ with a large azimuthal acceptance of about 85°.

[1]**R**ing **I**maging **CH**erenkov
[2]**M**ultiwire **D**rift **C**hambers
[3]**M**ultiplicity and **E**lectron **T**rigger **A**rray
[4]**R**esistive **P**late **C**hamber
[5]**T**ime **O**f **F**light

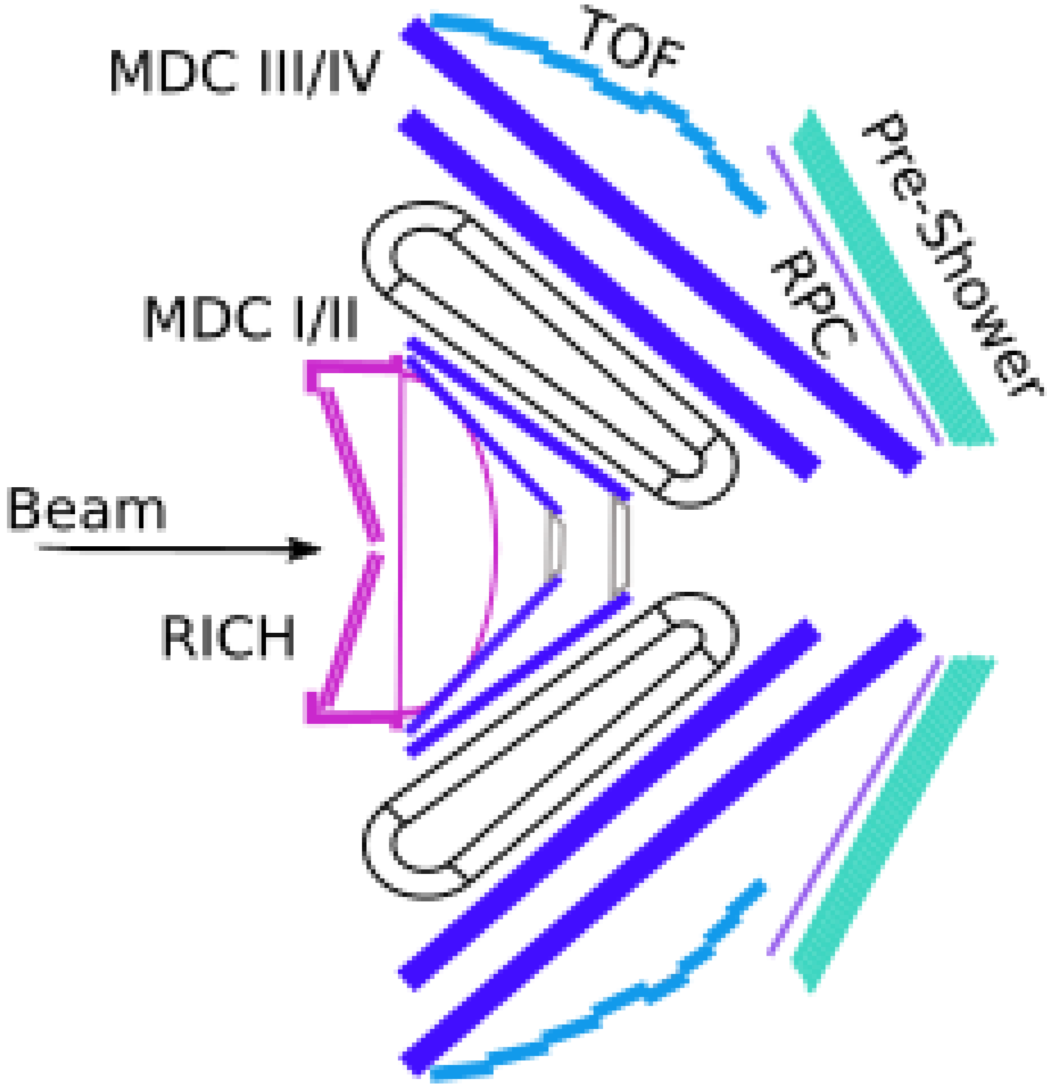

FIGURE 2.1: Overview of the HADES detector assembly. The pion beam coming from the left side of the figure gets detected by START and hits the target. In the following, the reaction products transvers the RICH, which is used to discriminate electrons from hadrons. Particle tracking and therefore the momentum reconstruction is performed with the MDCs, in front and behind the superconduction toroidal magnet. The RPC and TOF are part of the time of flight measurement, while also being valueable for the electron-hadron discrimination and the hadron multiplicity. At last, electromagnetic shower processes can be observed with Pre-Shower. [3]

2.1 Secondary Pion Beam

Secondary pion beams are generated along with other particles (eg. protons) by primary proton, ^{12}C or ^{14}N beams impinging on a beryllium target in front of the HADES setup. The pion beam is focused by quadrupole magnets, while dipole magnets select the pions through their deflection angle. The acceptance of the beam optics leads to a momentum resolution of $\Delta p/p = 8\%$. To achieve a better momentum resolution, the pion tracker CERBEROS[6] has been installed. It consists of two silicon detectors combined with the beam optics transport code, which measure the momenta of the pions with a resolution better than the demanded $\Delta p/p = 0.5\%$.[9]
The selected data for the following analysis had an incident π^- momentum of 1.7 GeV / c.

2.2 Carbon-Target

The carbon-target employed during the pion beam campaign is shown in Fig. 2.2.
The target is divided into three segments. Each segment has a diameter of 12 mm, with a length of 7.2 mm. A carbon tube sustains the target as shown in the figure.[10]

2.3 START-Detector System

The START-detector is placed in front of the target to determine the reaction time T0 as well as to observe the beam properties and quality of the beam. Since T0 is part of the Time of Flight measurement, which is used for particle identification and particle identification, a high precision of $\frac{\Delta T}{T}$ is needed. During the pion beam the detector consisted out of 9 scCVD (Chemical Vapour Deposition) diamond elements.[3][2]

2.4 RICH-detector

The **R**ing **I**maging **CH**erenkov (RICH) technique is used to discriminate electrons and positrons from hadrons. Particles with velocities faster than the in-medium speed of light create Cherenkov radiation inside the radiator. At SIS18 energies, $\beta = \frac{v}{c} \approx 1$ for leptons, while it has values of $\beta < 0.95$ for hadrons. Thus, those hadrons do not produce a Cherenkov light cone, which ensures the measurement of only e^-/e^+.[2]

[6] Central Beam Tracker for Pions

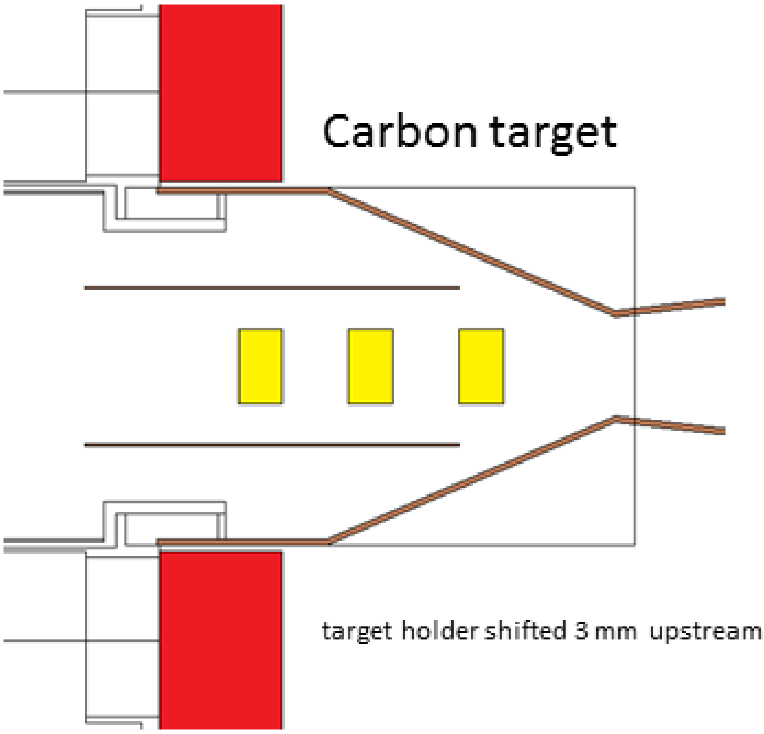

Target	Diameter [mm]	Seg. length [mm]	zLab of seg. centers [mm]
Carbon	12	7.2	-52.1, -34.1, -16.1

Target holder:
carbon-fibre tube with outer diameter of 26mm and wall thickness of 0.5 mm

FIGURE 2.2: The geometry of the used target. Carbon was used as target for the negative pion beam. The Carbon-target consists of three smaller segments, as depicted, with a diameter of $12\,\mathrm{mm}$ and a segment length of $7.2\,\mathrm{mm}$.[10]

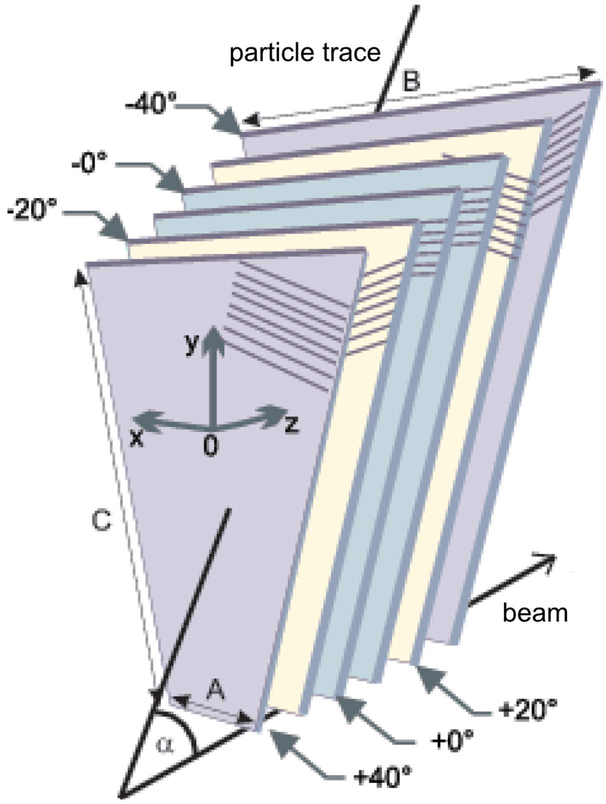

FIGURE 2.3: Setup of one MDC module. Illustration showing the six anode wire frames. The angles noted in the picture describe the tilt of the wires inside the planes. [3]

2.5 MDC-Detectors and the Magnet

The momentum of the produced particles is reconstructed by measuring the deflection angle of the particle trajectories after transversing the magnetic field.
Hence, from the hit positions in the **M**ultiwire-**D**rift-**C**hambers (MDCs) the particle tracks are reconstructed. In total, there are four drift chambers, two in front and two behind the magnet; each one of them is made of six trapezoidal modules. Every module covers 60° of the azimuthal angle and is composed out of six drift cell layers as pictured in Fig. 2.3. Cathode wire planes and interspersed sense and field wires form the cells.

To obtain the momentum, the track is calculated using a transverse kickplane. Further, the matching for the electron identification with RICH requires a alomost field free region around the target. Moreover the magnet was built such that the MDCs can cover a momentum range from $0.1 - 2\,\mathrm{GeV}/\mathrm{c}$ and a polar angle from $\theta = 18 - 85°$ leading to a strongly inhomogeneous field.
The coils of the magnet are surrounded by a nitrogen cooled shield at $88\,\mathrm{K}$ to obtain temperatures at which they are superconducting. [2]

2.6 META-system

The **M**ultiplicity and **E**lectron **T**rigger **A**rray (META) system consists of both the **R**esistive **P**late **C**hambers (RPC) and the **T**ime **O**f **F**light (TOF) detector. By combining the time of flight with the in the MDCs provided momentum obtained by the matching system and the energy loss determination, one can distinguish electron-hadron discrimination and measurement of hadron multiplicities.[2]

Both detectors are divided into six sectors following the hexagonal symmetry of the whole spectrometer. The RPC is the upgraded inner TOF wall, replacing the TOFino. It covers polar angles from 18° to 44°, while the TOF detector is responsible for polar angles from 44° to 80°. While the TOF is a scintillator, where particles generate flashes of light, which are measured with amplification through photo-multipliers, the RPC is a resistive plate chamber, made of kathode and anode plates and resistor material. [3]

2.7 Trigger

HADES features a two-staged trigger system to reduce the amount of purely hadronic events, which can be used to enhance the electron yield.

The digital level-1 (LVL1) trigger signal is created by the CTU[7]. In parallel, a common start signal is sent to all sub-detectors, with the CTU locked until all DTUs[8] have released the trigger bus. Hence, the trigger system is not dead time free and the rate of accepted triggers is depending on the readout capabilities of the sub-systems. Nevertheless, this approach ensures that only complete events are accepted by the trigger system without any missing data. [3]

The trigger inputs of the LVL1 trigger can be separated in two different classes. The calibration triggers ensure adequate performance of the detectors during the digitisation progress, while the physics triggers are coming from the START[9] detector. [3]

The LVL2 trigger was implemented to sort the events for included di-electron pairs through signatures ind RICH (Cherenkov rings), TOF (fast particles) and the Pre-Shower (electromagnetic showers). For the experiment discussed in this paper, the only requirement for the LVL1 trigger was a multiplicity of two in the TOF and RPC detectors, as pure hadronic reactions were also of interest for the analysis. [3]

[7] **C**entral **T**rigger **U**nit
[8] **D**etector **T**rigger **U**nits
[9] If START is missing from the first particle hit in TOF/RPC

3 UrQMD and GiBUU transport models

In the field of modern nuclear physics exotic and rare channels get in the focus of interest. To disentangle between the different contributions arising from various reactions inside the nucleus, one has to rely on simulations or partial wave analysis. An excellent description of the different stages of the reaction is necessary, as these simulations also are used for the correction of the experimental data. One way to test the accuracy of these simulations is to take a simultaneous look at the simulated and experimentally obtained and recorded particle yields.

In the following analysis, two different microscopic transport models were applied and compared: the **U**ltra**r**elativistic **Q**uantum **M**olecular **D**ynamics (UrQMD) model [11] and the **Gi**essen **B**oltzmann-**U**ehling-**U**hlenbeck (GiBUU) project [7].

Microscopic transport models are used for the description of all kinds of nuclear reactions. Thereby, the production and propagation of particles are simulated in a time-dependent framework taking into account in-medium effects (e.g. rescattering, absorption). Such models are not only applicable for the interpretation of experimental data, but also offer some predictive power. Moreover, they serve as an event generators for later on performed corrections of the experimental data (e.g. detector efficiency).

3.1 UrQMD transport model

The UrQMD microscopic transport model was developed to describe (ultra)relativistic heavy-ion collisions. The model can be applied in the energy regime from SIS18 (this thesis $\sqrt{s}_{\pi N} = 2\,\mathrm{GeV}$) to the RHIC[1] energies ($\sqrt{s}_{NN} = 200\,\mathrm{GeV}$). The key component of the model is the description of particle creation and evolution in dense hadronic matter at high temperatures allowing to apply this model to a huge variety of topics, including

[1]**R**elativistic **H**eavy **I**on **C**ollider at the Brookhaven National Laboratory

mesonic matter, antimatter production or the transport of rare particles in hadronic matter. [4]
UrQMD uses a Monte Carlo approach to describe the motion inside the medium and the creation or destruction of the particles. Especially, it is based on covariant propagation of all hadrons on classical trajectories, combined with stochastic binary scattering processes, formation of color strings and decay of resonances.[11]
The application of Monte Carlo methods leads to the solution of large sets of coupled partial integro-differential equations for the time evolution of various phase space densities $f_i(x, p)$ of particle species i. The phase space densities non-relativistically follow the Boltzmann form.

The collision term of a particle species, connected to any other particle species, includes 55 baryon species and 32 mesons. [11]
To assure full baryon-antibaryon symmetry, the antiparticles have been implemented through charge conjugation.[11]
The basic input to the UrQMD model are the particle species and energy-dependent cross sections of elementary interactions. The total cross sections are implemented geometrically.[11]

3.2 GiBUU transport model

The GiBUU project was designed in Giessen and was developed for numerical solutions of nuclear reactions in the MeV and GeV energy regimes, such as e^{-}+A, γ+A, ν+A or h+A[2], as well as for A+A.[7]
This unified theory and transport framework can describe the reaction fully and dynamically and delivers the event's complete final state.[7]
On the basis of the BUU-equation the collisions and propagation of particles in a mean field over the spacetime evolution of the phase-space density is described.[7] In the BUU-equation, the hadronic and Coulomb mean fields as well as the "off-shell" potential are included, and the collision term C accounts for decays and scattering processes.[7] To guarantee the locality in scattering processes of the test particles, the solution relies on a test particle ansatz in a full ensemble scheme. [7]
GiBUU is semi-classical and a purely hadronic model, containing 90 baryonic and 34 mesonic states. Not all quantum effects are implemented. [7]
The wanted quantities are mostly the cross-sections for collisions between the known states for every energy regime and the mean-field potentials for the different particle

[2]Especially p+A and π+A

species. The model relies on measured reaction cross sections and mean field potentials for different particle species which are often not well known. [7]

UrQMD	GiBUU
many-particle-ansatz	single-particle-ansatz
Seperate view on single particles through coupling of the equations of motion	Interaction of particles over a mean field
Solution of the Boltzmann-equation	Solution of the Boltzmann-Uehling-Uhlenbeck-equation
Many-particle correlations possible	Calculation of the single-particle distributions at each time from the state of all particles. No many-particle correlations.
Superposition of single-particle distributions $\rightarrow$ Total distribution function	Averaging of the parallel-ensemble $\rightarrow$ Total distribution function
$\sqrt{s} < 2.0\,\mathrm{GeV}$: resonance model	$\sqrt{s} < 3.4\,\mathrm{GeV}$: decay of resonances
$\sqrt{s} > 2.0\,\mathrm{GeV}$: PYTHIA-event generator	$\sqrt{s} > 3.4\,\mathrm{GeV}$: PYTHIA-event generator
32 mesons	34 mesons
55 baryons	90 baryons

Table 3.1: Characteristics and differences between the GiBUU and UrQMD approaches for many-particle functions [13]

4 Analysis Procedure

4.1 Cuts on the p-β-Spectrum as Particle Identification

In the beginning of the data analysis the particle species needs to be determined. For this the specific beta-momentum relation is used with $\beta = \frac{v}{c}$:

$$\beta(p) = \sqrt{\frac{p^2}{(mc)^2 + p^2}} \tag{4.1}$$

The characteristic difference for the different particle species at a given momentum is their mass. For charged pions, the mass equals 139.6 MeV/c^2. Therefore, a characteristic curve as shown in Fig. 4.1 can be plotted. As both charged pions have equal mass for particles and antiparticles, their behaviour in the p-β-spectra is equivalent.
Fig. 4.1 displays all negative (top) and positive (bottom) particles in the presented momentum range. In the top figure, the negative pions are distributed around the theoretical curve, while electrons and myons can be identified at low momenta and high beta values. Additionally, protons and deuterium closer to the momentum axis.
As the detector has a finite resolution, the p-β-relation gets smeared. To determine the exact width of the curve, the spectrum can be sliced into momentum bins of 100 MeV / c and projected to the y-axis. The resulting distributions show the β-value of different particles for a given momentum range. An example for such a distribution is illustrated in Fig. 4.2, showing the Gaussian peak of π^+ with a K^+ impurity, identified by the simulation pid, at lower β-values. Depending on the momentum range of the slice, different particle species smear inside the pion curve. For low momenta around 230 MeV / c to 370 MeV / c, the intruding particles can be identified as e^-/e^+ and μ^-/μ^+, while, especially for positive particles, K^+ and p^+ can be observed for higher momenta than 800 MeV / c.
To identify the pions, the whole curve has been fitted with a Gaussian for the pions plus a second order polynomial as background (ug). If other particles can be identified, their peaks have been plotted with an additional Gaussian. This fitting function can be seen in formula 4.2 and was applied in Fig. 4.2.

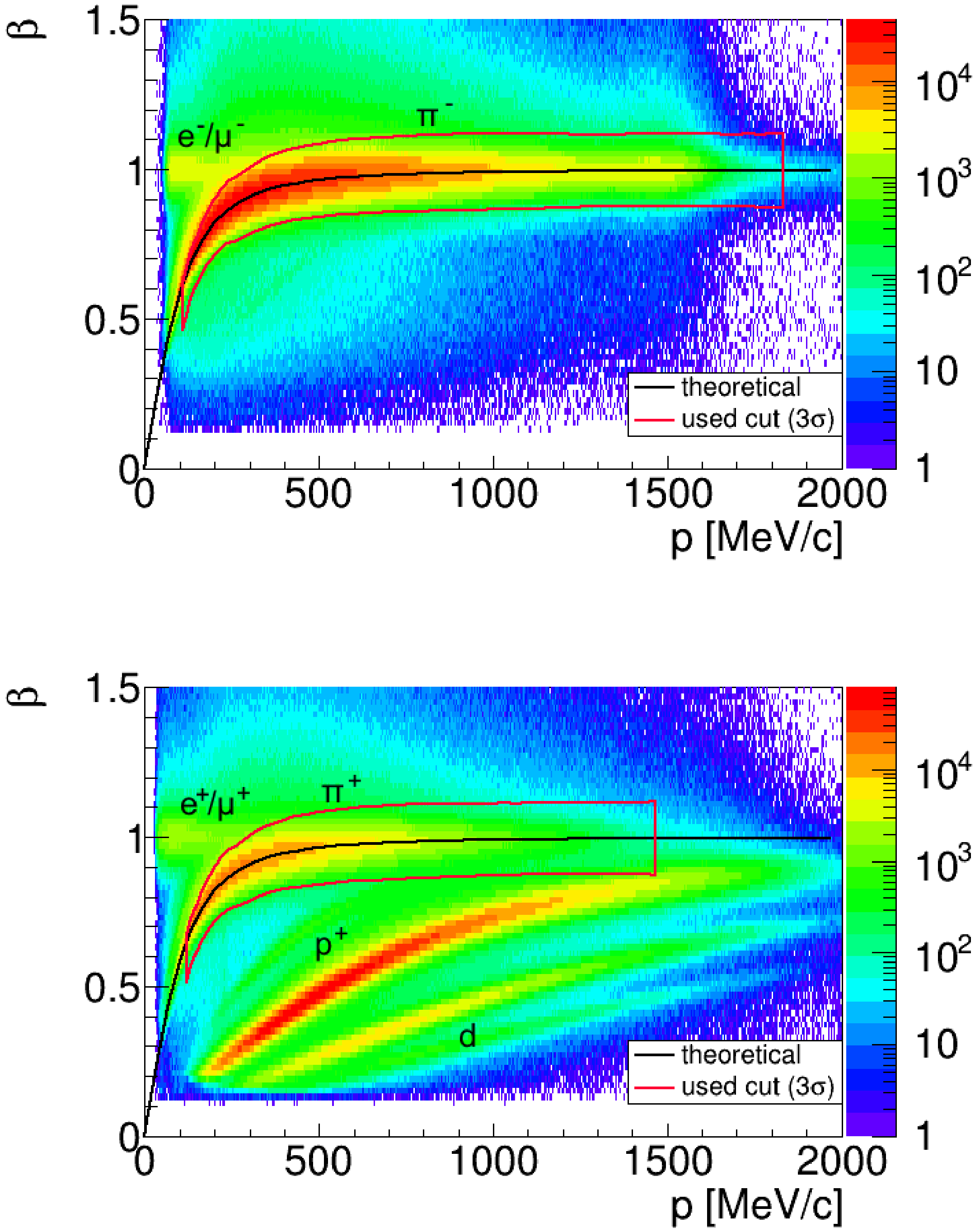

FIGURE 4.1: Particle velocity β as a function of the momentum for negative (top) and positive (bottom) charged particles. The black line corresponds to the theoretical velocity for charged pions. The red line indicates the applied 3σ cut for the pion selection.

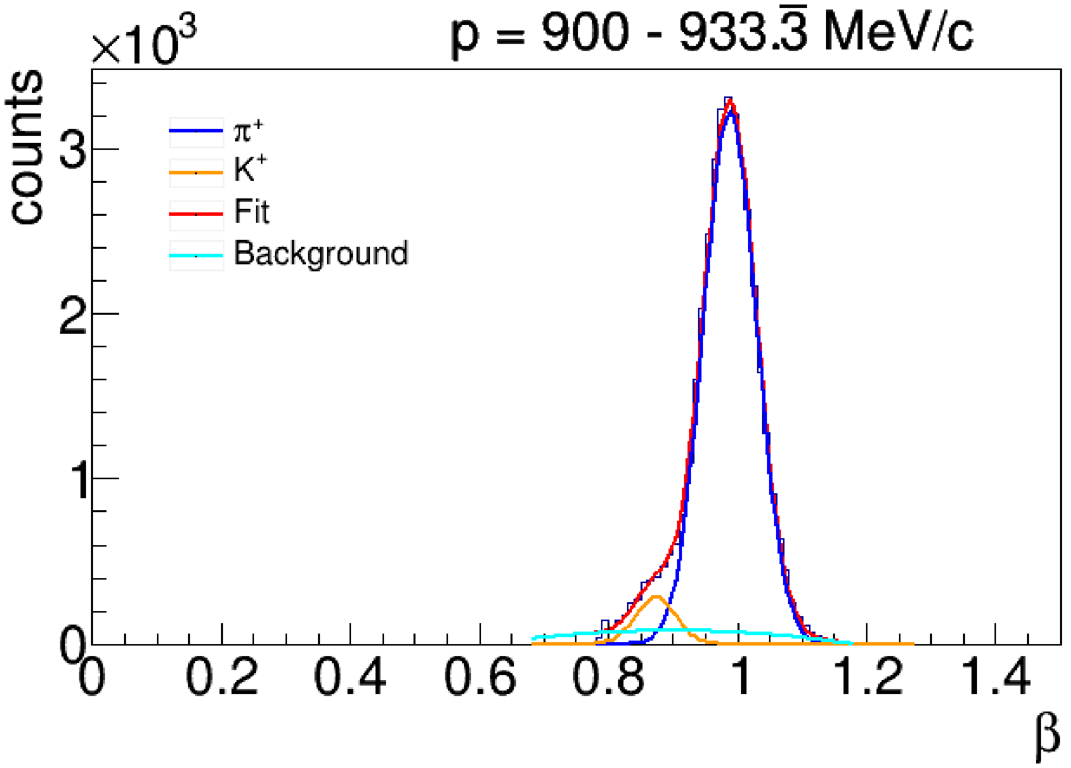

FIGURE 4.2: Example figure from UrQMD showing the particle distribution over β in a momentum range from $900\,\mathrm{MeV}\,/\,\mathrm{c} \leq p \leq 933.3\,\mathrm{MeV}\,/\,\mathrm{c}$. The overall fit (red) consists of the pion peak (dark blue), the kaon peak (orange) and the background (light blue).

$$y = a_\pi \cdot \mathrm{e}^{-\frac{1}{2}\cdot\left(\frac{x-\mu_\pi}{\sigma_\pi}\right)^2} + a_{ug} \cdot (x - z_1) \cdot (x - z_2) \left(+ a_{other} \cdot \mathrm{e}^{-\frac{1}{2}\cdot\left(\frac{x-\mu_{other}}{\sigma_{other}}\right)^2} + \ldots \right) \tag{4.2}$$

The first summand corresponds to the pion peak, with a_π the amplitude, μ_π the mean value and σ_π the parameter which describes the width of the peak. The following part was used to describe the background, which consists mostly of contributions of other particles which are not not separated well for a reliable description with a Gaussian. The parameters z_1 and z_2 are given through the zero-crossings of the distribution. The remaining summand has been applied to momentum regions, were significant Gaussian peaks of other particles could be identified by asking for the PID.
The resulting mean value μ_π of the pion peak was compared to the theoretical curve. For momenta higher than $250\,\mathrm{MeV}\,/\,\mathrm{c}$, the mean values μ_π resemble the theoretical curve well, while they show a slight difference for lower momenta reasoned by the energy loss correction.

To produce a cut which includes as many pions as possible while excluding most other particles, a range of $3\sigma_\pi$ around mean value μ_π has been used. For π^-, which were also the beam particles, momenta up to 1800 MeV / c could be accepted, while for the positive pions π^+ already for momenta of 1500 MeV / c no significant peak could be observed.
The resulting cuts are plotted in picture 4.1. The ones for the UrQMD and GiBUU transport models are shown in A in the Appendix.

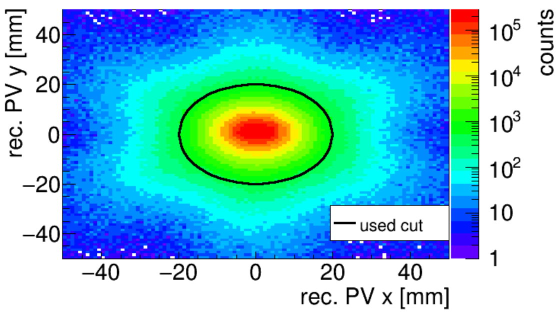

FIGURE 4.3: Reconstructed primary vertex in the x-y-plane. The selected region is indicated by the black circle.

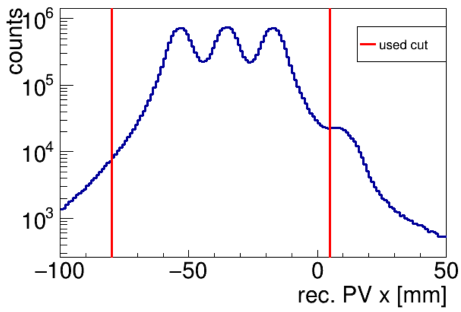

FIGURE 4.4: Reconstructed primary vertex parallel to the beam axis. The three peaks correspond to the target segments. A region from $-80\,\mathrm{mm}$ to $5\,\mathrm{mm}$ has been selected (black lines).

4.2 Cuts on the Reconstructed Primary Vertex

To assure that only events originating from reactions of the beam with the target are analysed, a selection on the reconstructed primary vertex[1] has been applied.

The primary vertex is reconstructed on the basis of at least two fully tracked particles, where the position measurement of the MDCs is combined with the z-coordinate information delivered by the META system (RPC/TOF).

Figures 4.3 and 4.4 show the primary vertex distribution for the x-y-plane and z-component, respectively.

The sixfold target structure arises from the spectrometer geometry. All events have to fulfill the condition of a transverse primary vertex position $R(x_{pv}, y_{pv}) \leq 20\,\mathrm{mm}$ indicated by the black circle.

[1]The primary vertex describes the original start of the trajectory of the measured particle

In Fig. 4.4 the three main peaks correspond to the target segments (see Sec. 2.2). Besides, a smaller fourth peak on the right side of the distribution is visible, which can be attributed to interactions of the beam with the beam pipe. Hence, a region between $-80\,\mathrm{mm} \leq z_{pv} \leq 5\,\mathrm{mm}$ has been selected to suppress reactions of the beam outside the target.

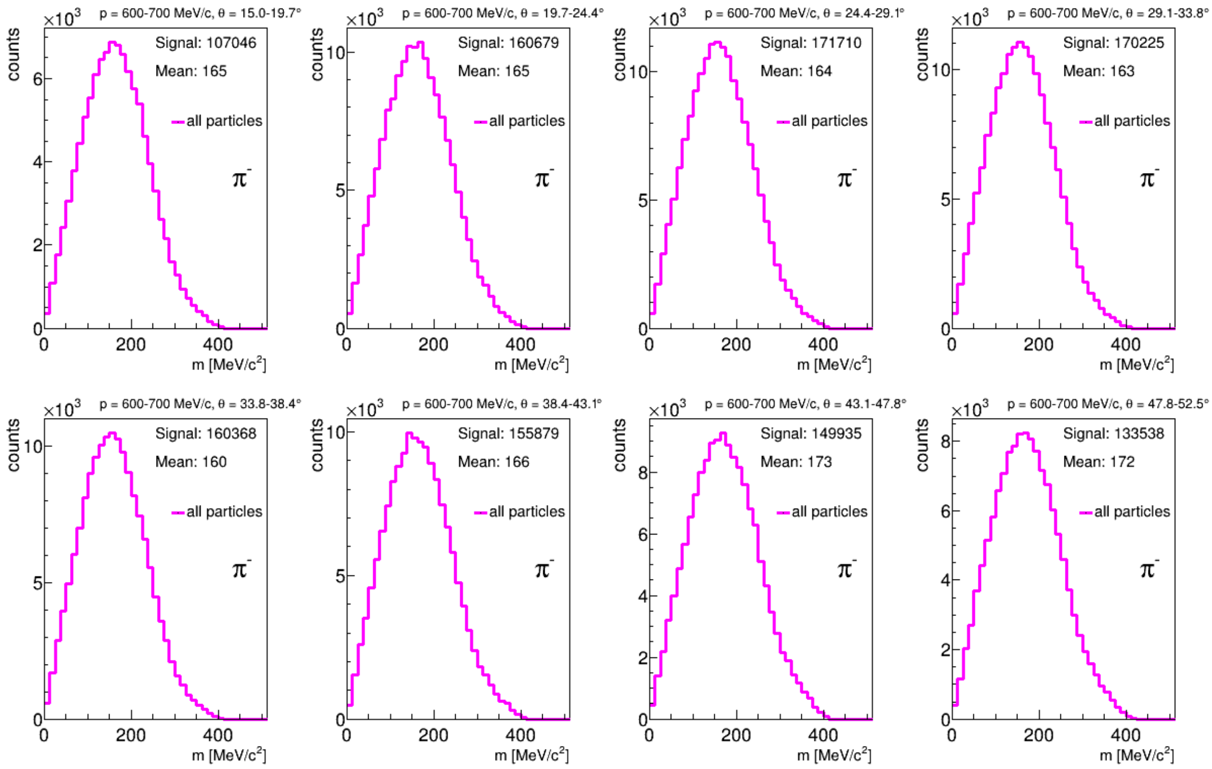

FIGURE 4.5: Experimental mass bins of π^- for momenta in the region of $600\,\mathrm{MeV\,/\,c} \leq p \leq 700\,\mathrm{MeV\,/\,c}$ and theta angles varying from $15° \leq \theta \leq 53°$. The mean values of the asymmetric Gaussian peaks are located at higher masses than the pion mass because of the high momentum leading to the measurement of a broad peak.

4.3 Mass Spectra in p-θ-Bins

The goal of the analysis are the pion yields and multiplicities which are derived in this section in p-θ-bins. The interval of $100\,\mathrm{MeV\,/\,c} \leq p \leq 1600\,\mathrm{MeV\,/\,c}$ has been cut into 15 bins, while the θ-interval of $15° \leq \theta \leq 90°$ was devided into 16 bins.

An example for the mass distribution in the momentum range of $600 - 700\,\mathrm{MeV\,/\,c}$ is shown in Fig. 4.5 for a θ-angle between 15° to 53°. Comparing these bins to UrQMD shows a good agreement, as illustrated in Fig. 4.6, which continues over the whole phase space. For the simulation, the pions are depicted as grey area, indicating a high purity.

The minimum pion mass is located at approximately $140\,\mathrm{MeV\,/\,c^2}$. For higher momenta the mass reconstruction decreases, leading to a broader peak as illustrated in fig. 4.5 and 4.6.

The yield has been determined by the integral of the different mass bin distributions, due to a high purity rather than fitting.

The plot below the mass spectra in fig. 4.6 shows the distribution of particles, which are

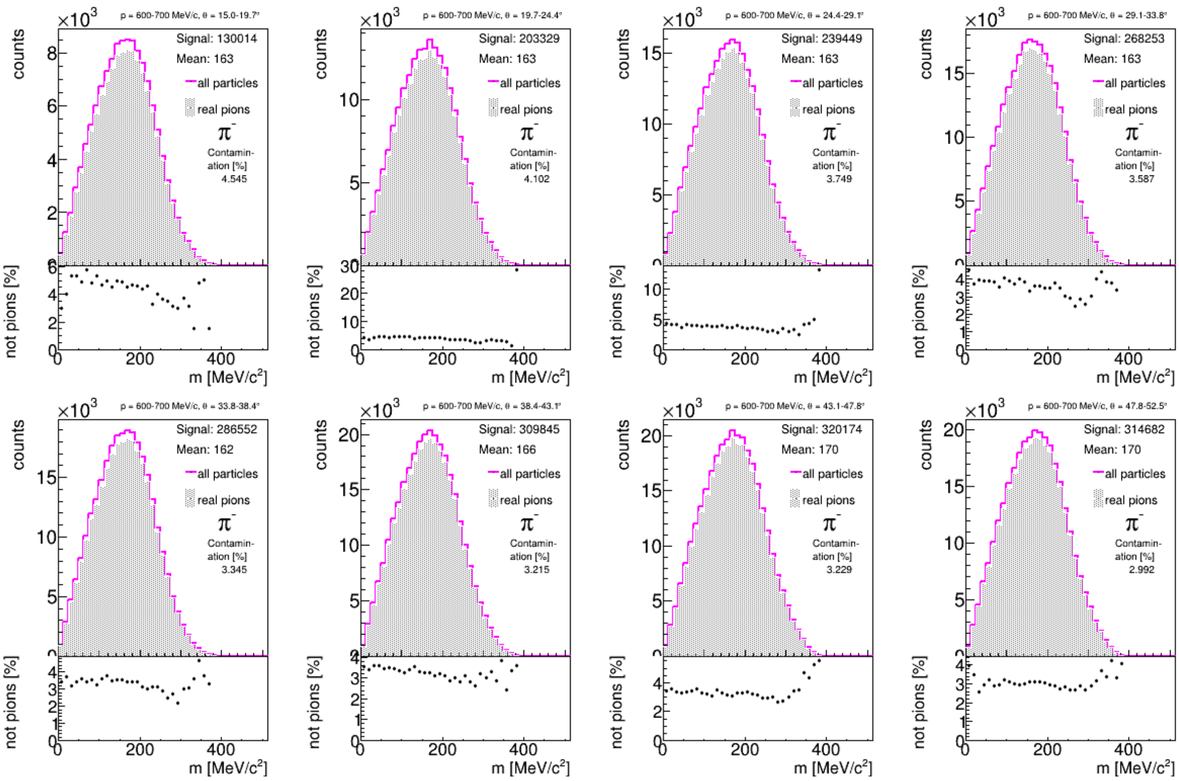

FIGURE 4.6: π^- mass distribution in UrQMD in the momentum region $600\,\mathrm{MeV}\,/\,\mathrm{c} \leq p \leq 700\,\mathrm{MeV}\,/\,\mathrm{c}$ and $15^\circ \leq \theta \leq 53^\circ$. The mean of the asymmetric Gaussians are located at higher masses than the nominal pion mass, because of the decreasing mass reconstruction at higher momenta. The lower graph illustrates the purity over the mass range in the bin.

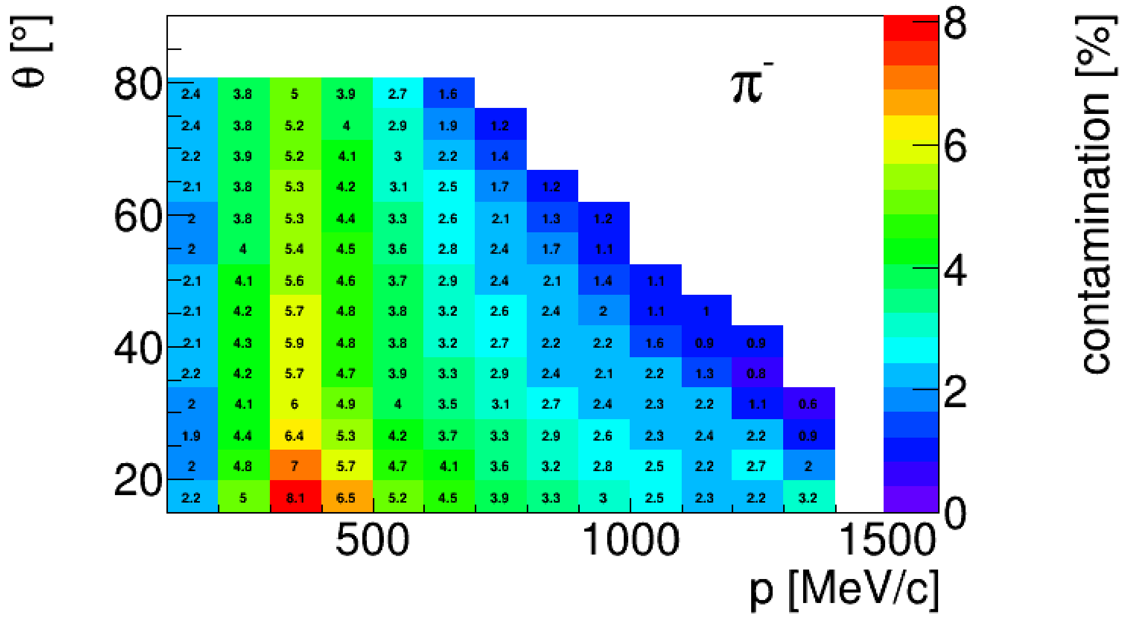

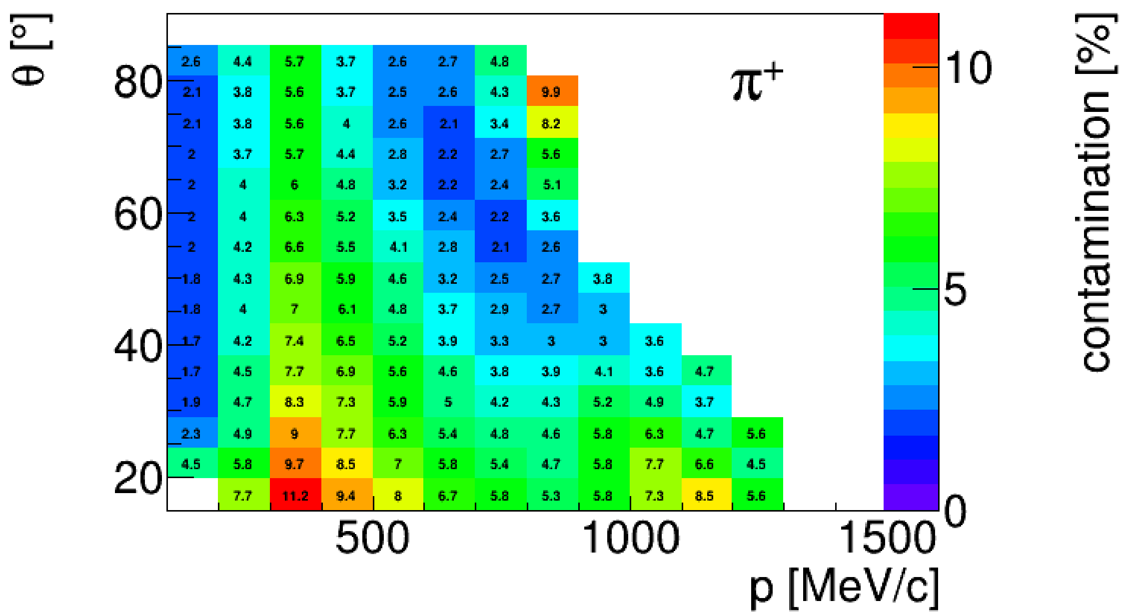

FIGURE 4.7: Contamination matrix for π^- (top) and π^+ (bottom) showing the percentage of particles inside the mass bins which are not pions. Nearly all bins with a contamination higher than 10% have been removed, as those bins weren't used for the later analysis. The contamination matrix has a peak at momenta around $300\,\mathrm{MeV}\,/\,\mathrm{c}$ and low θ coming from myons and partly electrons which could not be excluded by the analysis. As the statistic gets lower for high momenta and polar angles, those bins showed more fluctuation.

not pions in percent. Even if the number of misidentified particles rises for regions with vanishing statistics, the overall percentage stays low, as depicted in figure 4.7. At momenta around 300 MeV / c an increasing impurity is visible, arising from μ and e contamination. Overall, the π^- distribution shows a cleaner sample in comparison to π^+. Bins with more than 10% impurity have been excluded from the analysis, as well as those with low statistic. For π^+ more bins had to be eliminated, due to a higher contamination with protons.

Finally, the experimental yields shown in figure 4.8 were achieved. The ones for the negative pions are, as expected, higher, especially for higher momenta and low polar angles, were possibly the elastic scattered beam particles can be seen.[2] The overall particle yield is shown in Tab. 4.1.

p-θ	π^-	π^+
Uncorr. Yield N_{uncorr}	$2.174 \cdot 10^7$	$8.502 \cdot 10^6$

Table 4.1: p-θ uncorrected yield.

[2]The yields for UrQMD can bee seen in Sec. 4.5. Those were later used for the efficiency correction.

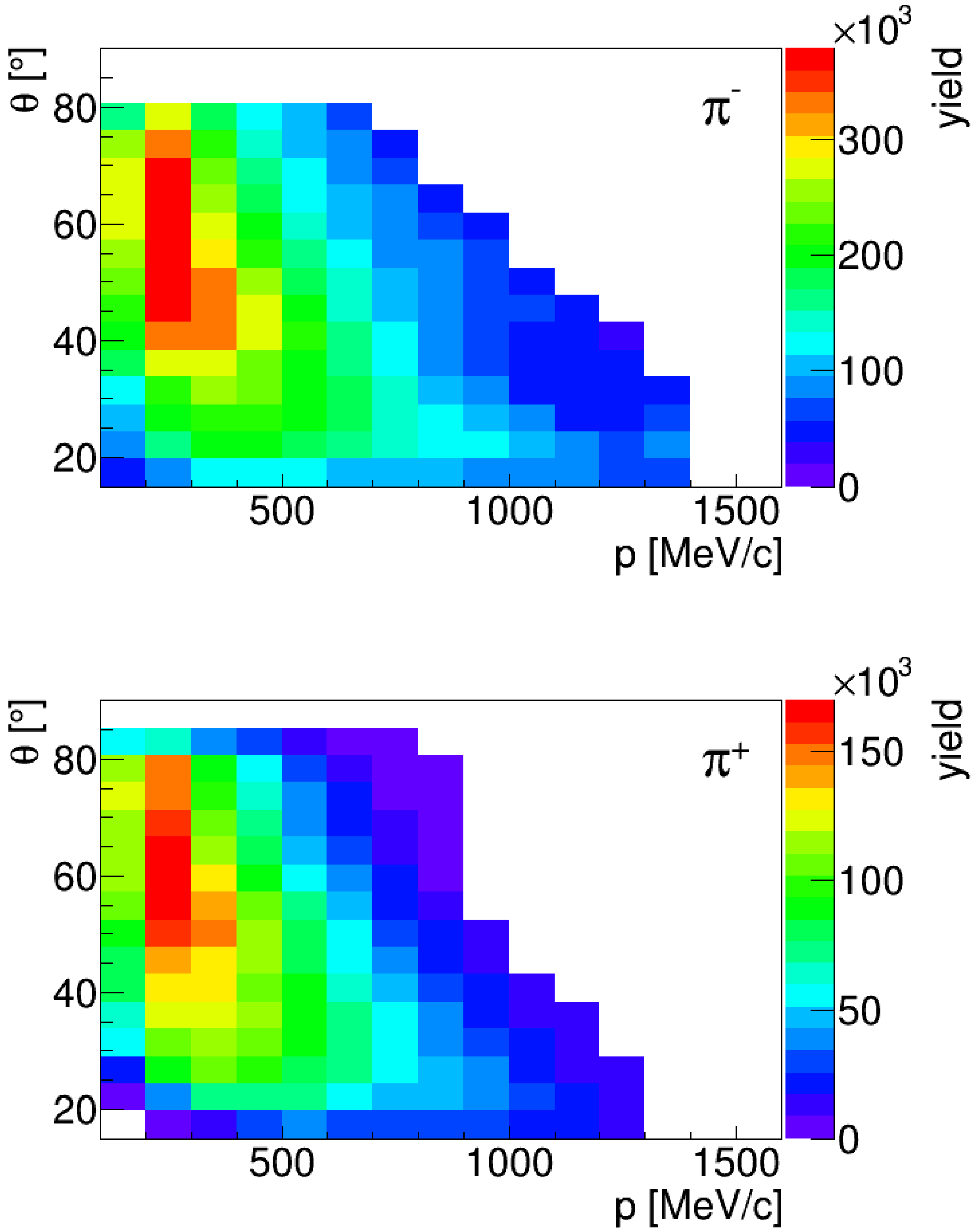

FIGURE 4.8: Yields of π^- (top) and π^+ (bottom) distributed over different momenta and polar angles. The yields for π^- are overall higher and especially show a peak at high momenta and low polar angles, due to elastic scattering.

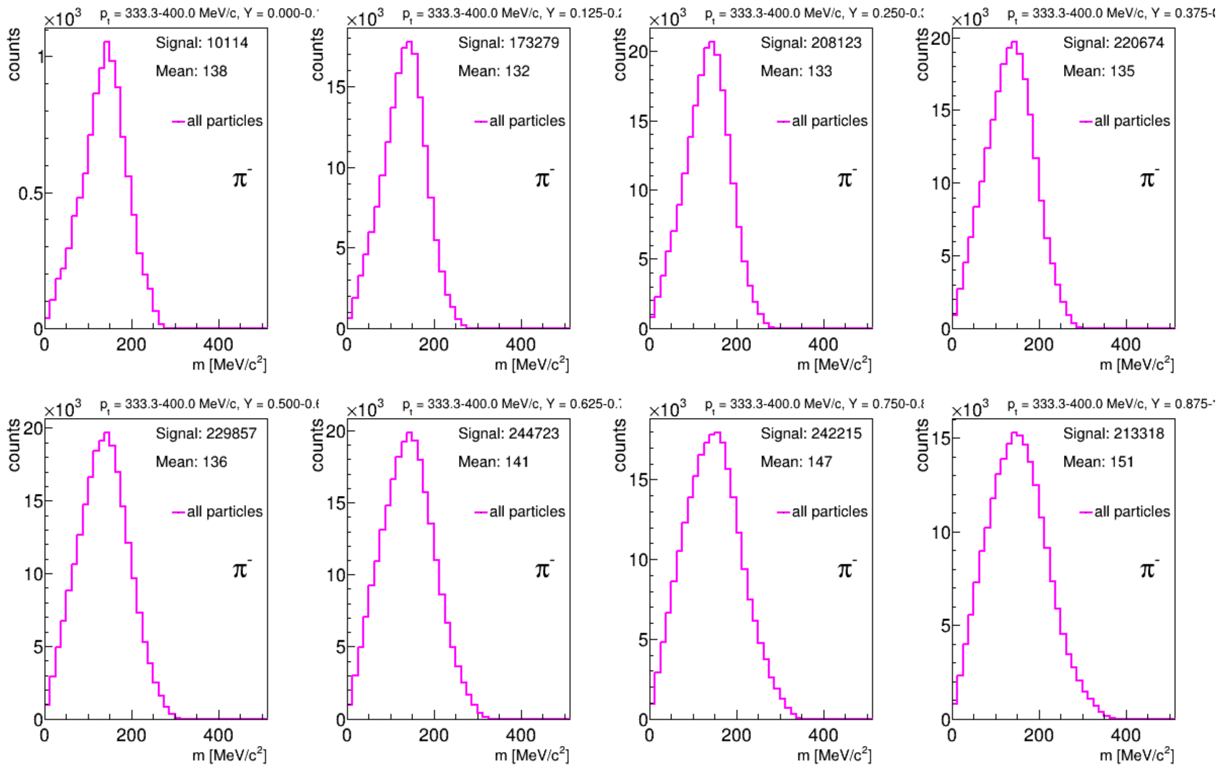

FIGURE 4.9: Experimental mass bins for transverse momenta in the region of $333\,\mathrm{MeV\,/\,c} - 400\,\mathrm{MeV\,/\,c}$ and rapidities varying from 0 to 1. For these peaks, the mean value does not only rise for high momenta but also significantly for high rapidities.

4.4 Mass Spectra in p$_t$-Y-Bins

The same analysis procedure as for p-θ-mass bins could also be applied for a different phase space. There, the dataset is divided into transverse momenta p_t and rapidities y. p_t ranges from $0 - 1000\,\mathrm{MeV\,/\,c}$, while y was observed for regions between 0 and 2. The distribution is divided into 15 equally sized bins for p_t and 16 bins for y.
Fig. 4.9 shows exemplary the distributions for $333\,\mathrm{MeV\,/\,c} \leq p_t \leq 400\,\mathrm{MeV\,/\,c}$ and $0 \leq y \leq 1$.
Similarly to p-θ, the mean values rise for higher transverse momenta, but do also show a dependence on the rapidity, as they rise for higher y.
Figure 4.11 shows the background contamination for the p_t-y-bins for π^- and π^+. Bins with higher transverse momenta are more contaminated than those with lower p_t, the same relation applies to the rapidity. The peak at low p_t and high y is reasoned by muons and electrons which could not be excluded in the analysis. Bins with a percentage of other particles than pions with a contamination higher than 10% have been excluded as well as the ones with low statistics.

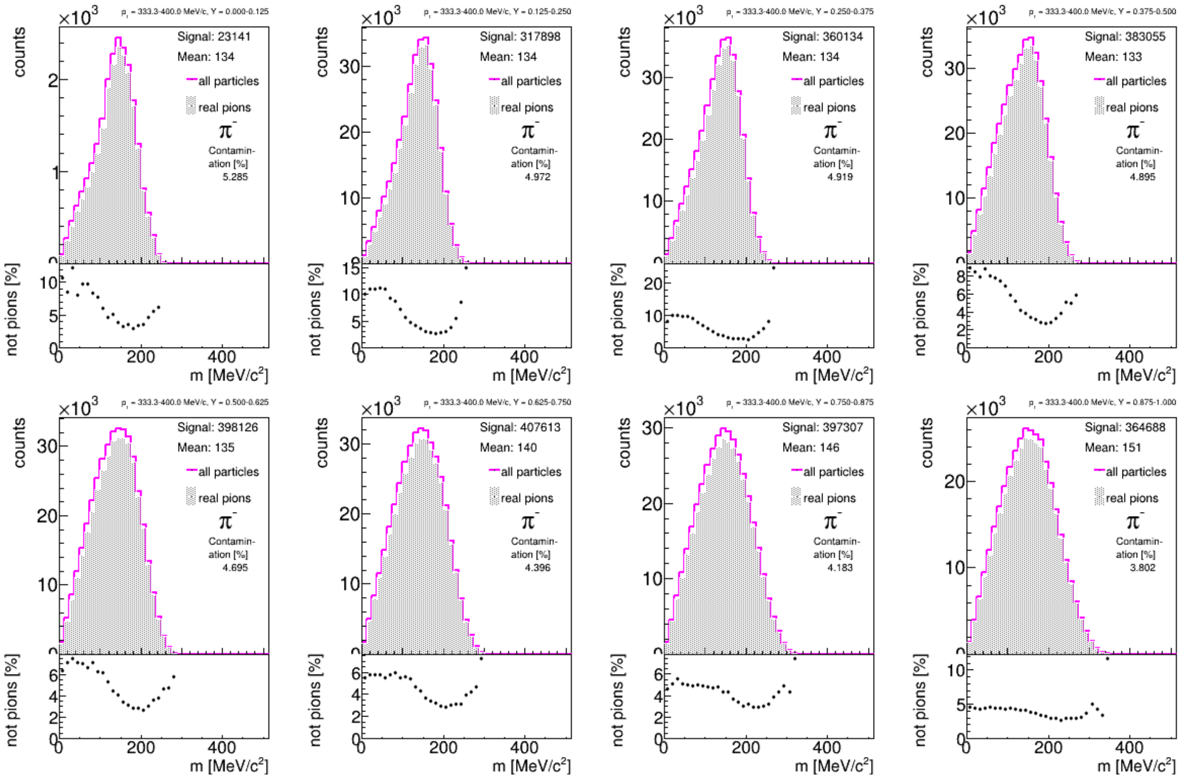

FIGURE 4.10: Mass bins created with UrQMD for transverse momenta in the region of $333\,\mathrm{MeV} / \mathrm{c} - 400\,\mathrm{MeV} / \mathrm{c}$ and rapidities varying from 0 to 1. For these peaks, the mean value does not only rise for high momenta but also significantly for high rapidities. The graph below the spectra shows the contamination percentage.

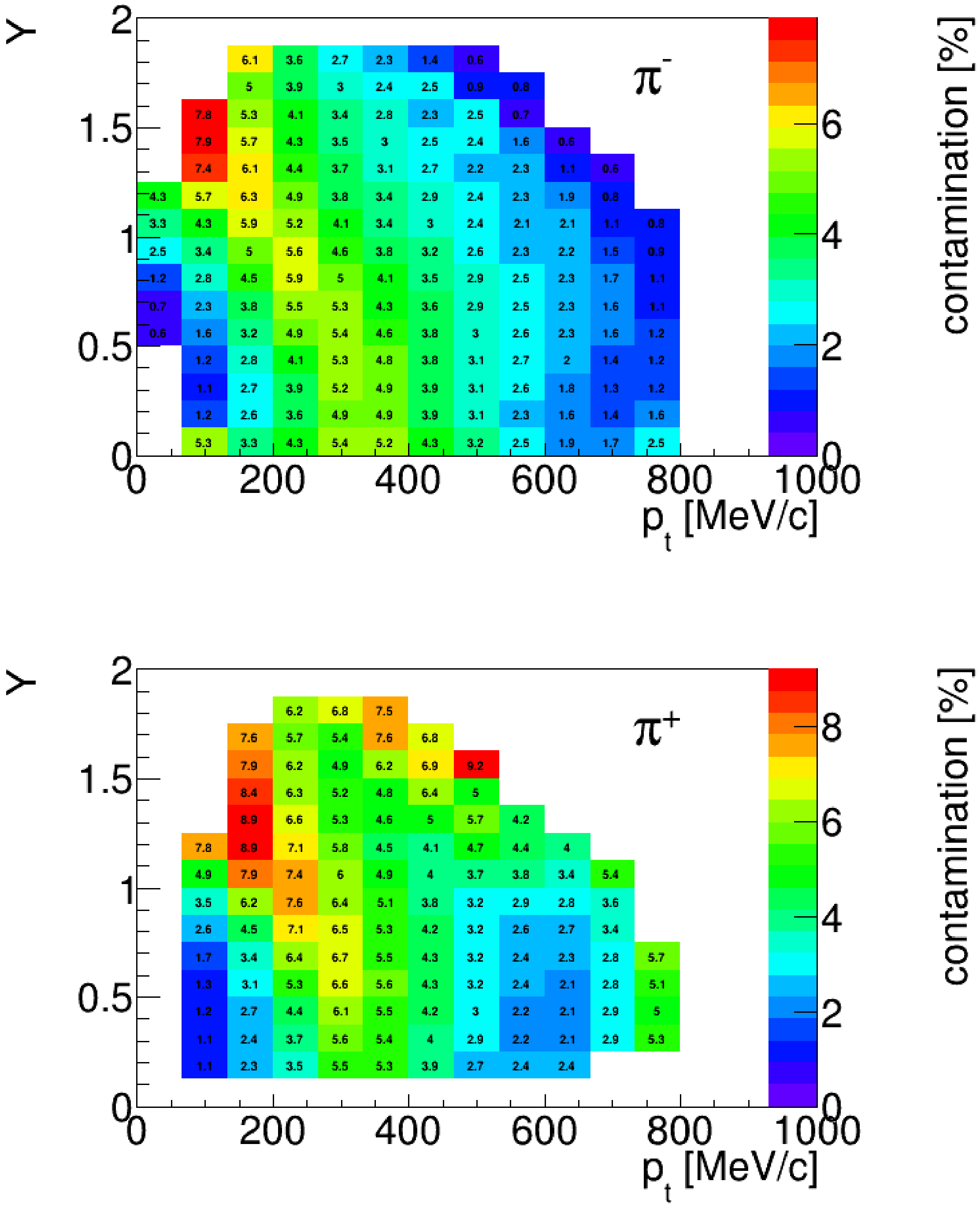

FIGURE 4.11: Contamination matrix for π^- (top) and π^+ (bottom) showing the contamination percentage inside the p_t-y-mass bins.

As the purity of the remaining bins is sufficiently high, the data could be used without any additional procedure.
The experimental yields[3] are plotted in fig. 4.12. The ones for π^- are higher than the ones for π^+ and possibly show an elastic scattering peak at 500 MeV / c and high y. The overall particle yields are shown in Tab. 4.2.

p_t-Y	π^-	π^+
Uncorr. Yield N_{uncorr}	$2.240 \cdot 10^7$	$8.323 \cdot 10^6$

TABLE 4.2: p_t-Y uncorrected yields.

[3]The yields for UrQMD, which were also used for the efficiency correction, can be seen in Sec. 4.5.

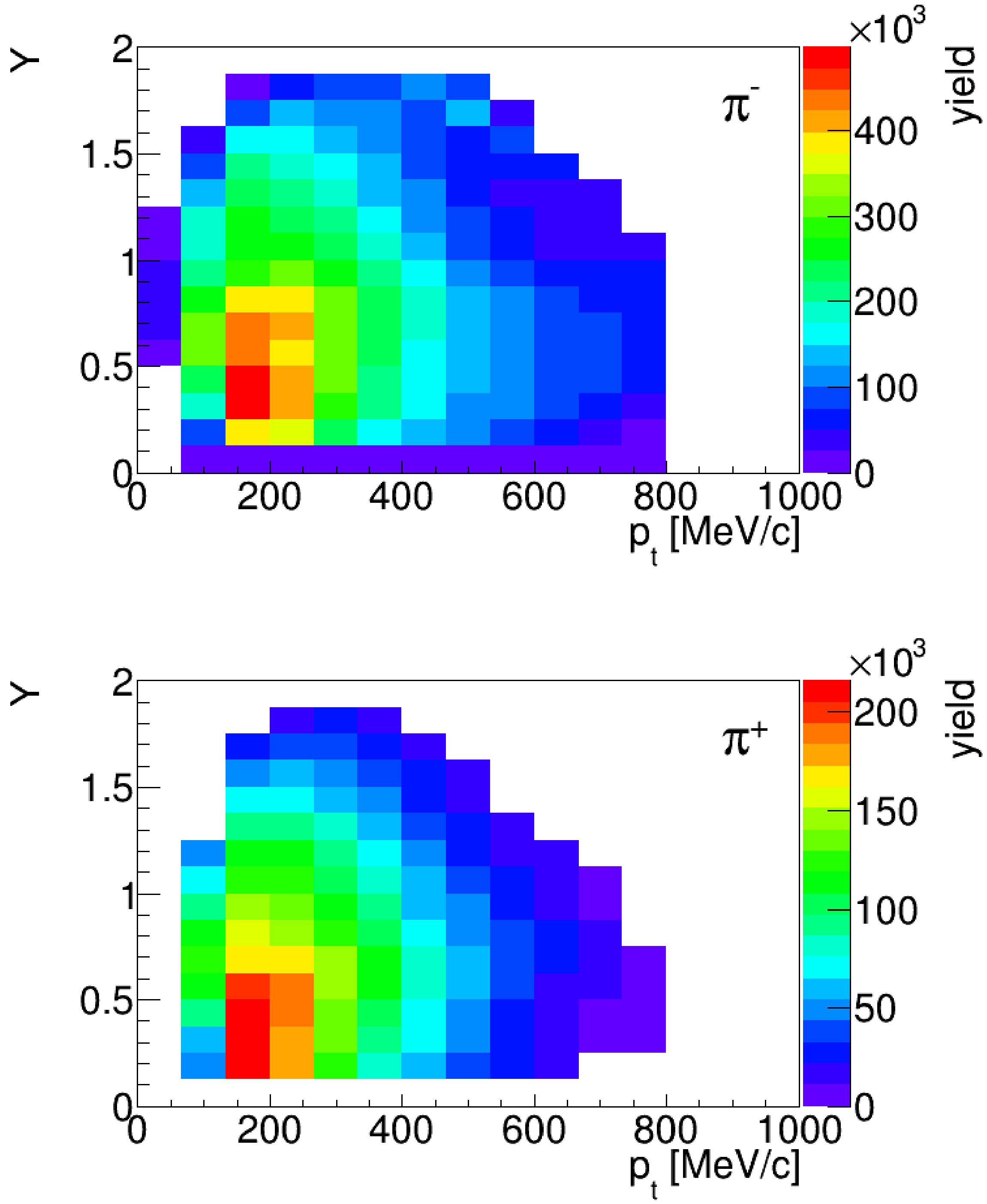

FIGURE 4.12: Yields of π^- (top) and π^+ (bottom) distributed over different transverse momenta and rapidities. For π^- they are overall higher than for π^+. At $p_t \approx 500\,\mathrm{MeV}/\mathrm{c}$ and high y for negative pions, the elastically scattered beam pions can be seen.

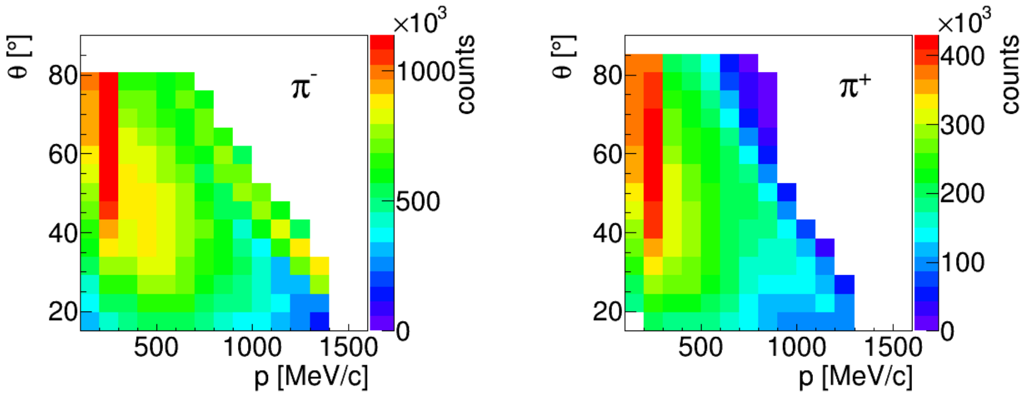

FIGURE 4.13: p-θ input matrices for UrQMD with π^- on the left and π^+ on the right side.

4.5 Efficiency and Acceptance Correction

p-θ	π^-	π^+
Uncorr. Yield N_{uncorr}	$2.174 \cdot 10^7$	$8.502 \cdot 10^6$
Corr. Yield N_{corr}	$5.760 \cdot 10^7 (\pm 1.235 \cdot 10^4)_{stat}$	$2.161 \cdot 10^7 (\pm 7.411 \cdot 10^3)_{stat}$

p_t-Y	π^-	π^+
Uncorr. Yield N_{uncorr}	$2.240 \cdot 10^7$	$8.323 \cdot 10^6$
Corr. Yield N_{corr}	$6.606 \cdot 10^7 (\pm 1.396 \cdot 10^4)_{stat}$	$2.054 \cdot 10^7 (\pm 7.120 \cdot 10^3)_{stat}$

TABLE 4.3: p-θ und p_t-Y uncorrected and corrected yields with statistical errors.

The recorded data needs to be corrected for the limited acceptance and efficiency of the HADES detector system. For this a dedicated sample was produced with the UrQMD transport code.
This sample has been used as an input for the HADES simulation framework, describing the propagation of the particles and the detector response. It has been analysed in the same manner as the experimental data.
By deviding the input shown in Fig. 4.13 and 4.14 and the output depicted in 4.15 and 4.16, the correction matrix is derived in p-θ and p_t-y. With this, the experimental yields could be corrected. Bins with low statistics are excluded, due to a low significance.
The output in Fig. 4.15 and 4.16 has obtained by the integral of the mass distributions for p-θ and p_t-Y as described in Sec. 4.3 and 4.4. With the input, the correction matrices in Fig. 4.17 and 4.18 could be obtained.
The uncorrected and corrected yields are depicted in Tab. 4.3. The statistical errors were

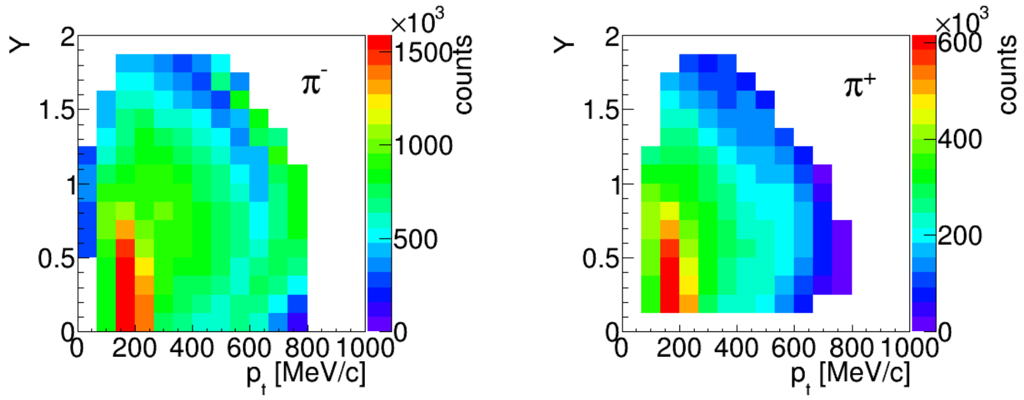

FIGURE 4.14: p_t-Y input matrix for UrQMD with π^- on the left and π^+ on the right side.

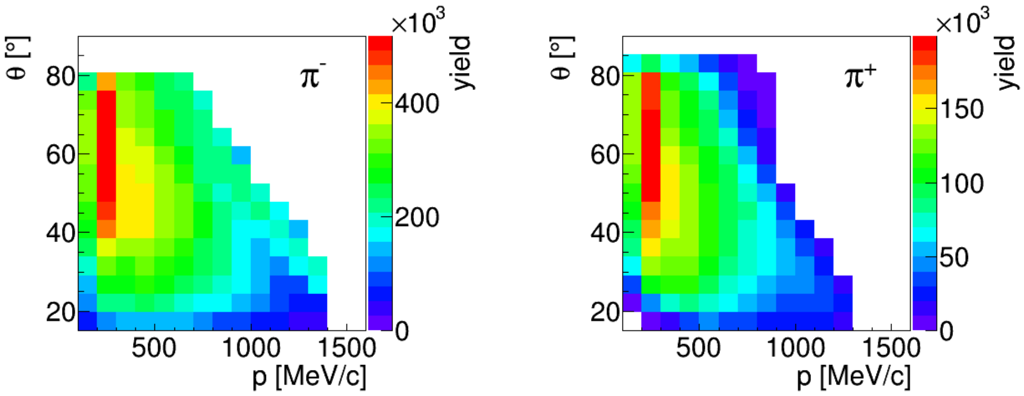

FIGURE 4.15: p-θ output matrices for UrQMD with π^- on the left and π^+ on the right side. The matrices have been achieved by integration of the p-θ mass distributions.

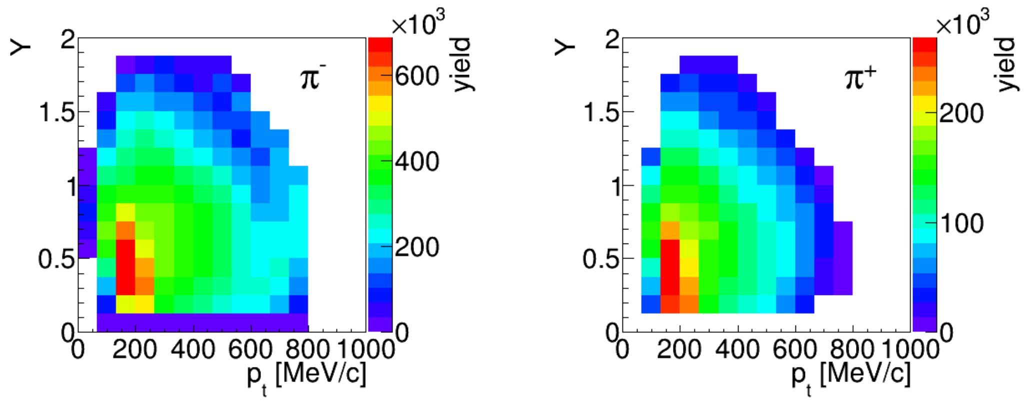

FIGURE 4.16: p_t-Y output matrices for UrQMD with π^- on the left and π^+ on the right side. The matrices have been achieved by integration of the p_t-Y mass distributions.

calculated as following:

$$\Delta N_{stat} = \frac{1}{\sqrt{N_{uncorr}}} \cdot N_{corr} \tag{4.3}$$

The statistical errors, which were calculated, are about three orders smaller than the yield values and do therefore not preponderate in comparison to the measurements.

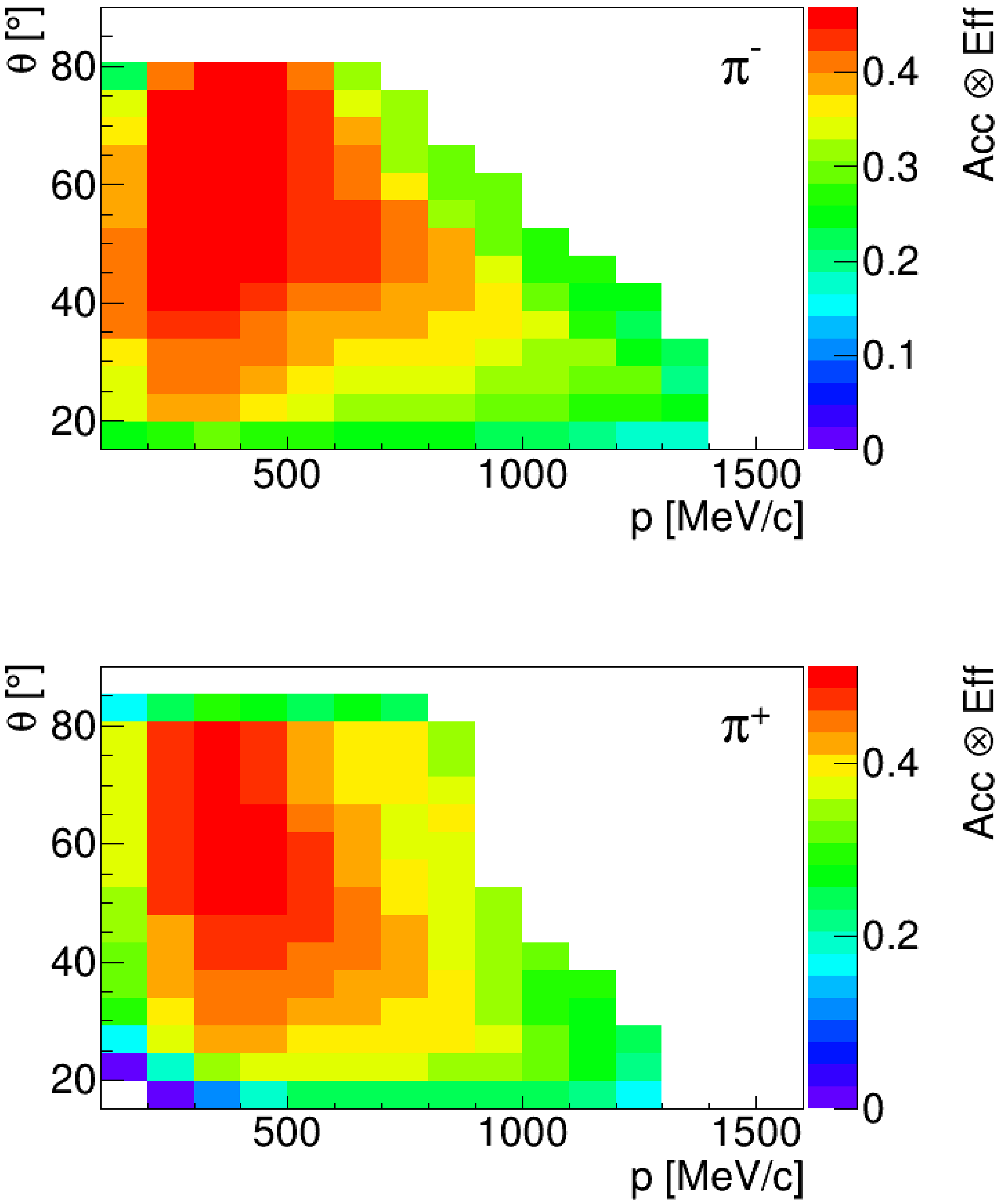

FIGURE 4.17: Efficiency and acceptance correction matrix for π^- (top) and π^+ (bottom) for the p-θ; created with UrQMD. The distribution is smooth and does not include correction factors higher than 1.

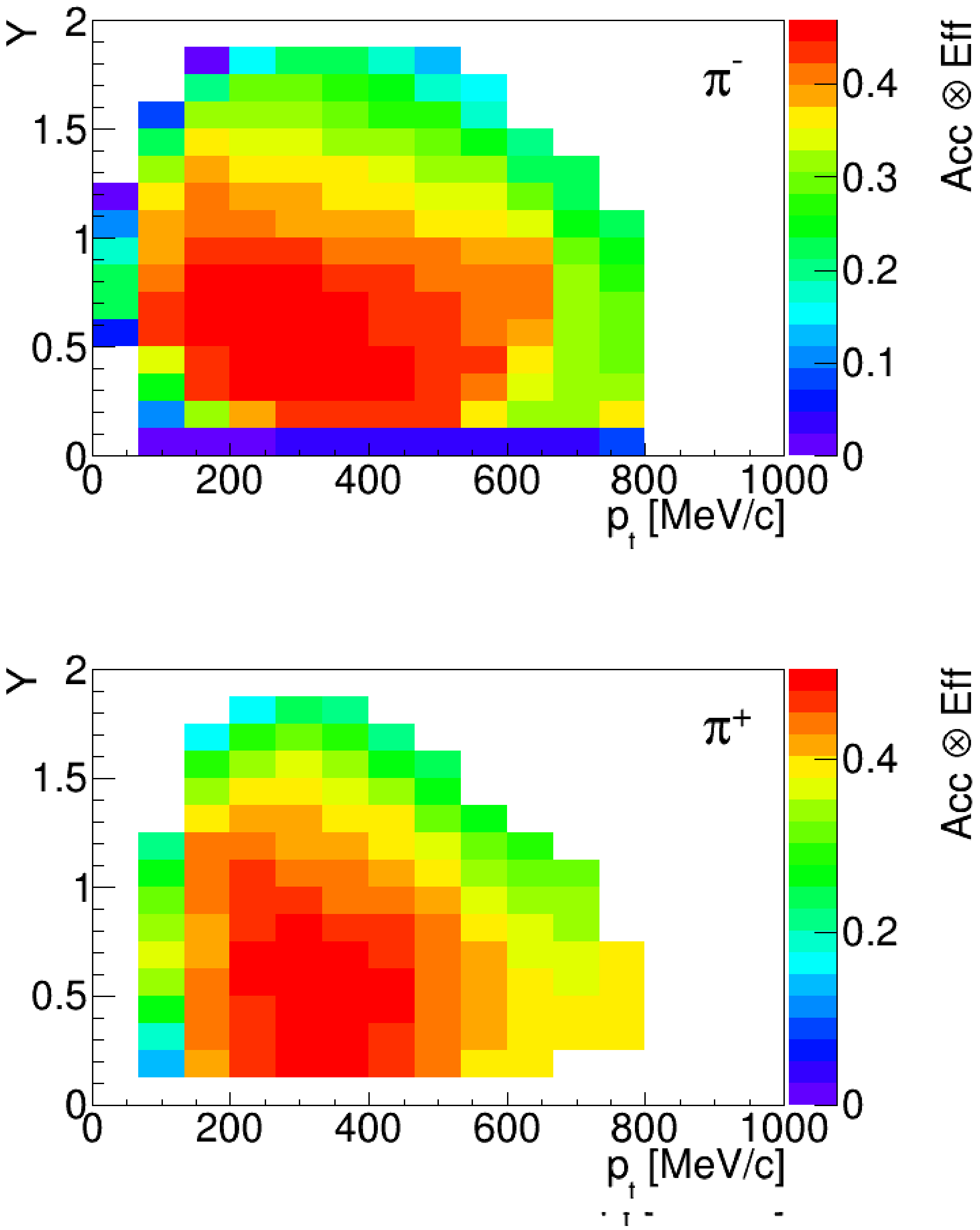

FIGURE 4.18: Efficiency and acceptance correction matrix for π^- (top) and π^+ (bottom) for the p_t-y; created with UrQMD. The distribution is smooth and does not include correction factors higher than 1.

p-θ	π^-	π^+
Uncorr. Yield N_{uncorr}	$2.174 \cdot 10^7$	$8.502 \cdot 10^6$
Corr. Yield N_{corr}	$5.760 \cdot 10^7 (\pm 1.235 \cdot 10^4)_{stat}$	$2.161 \cdot 10^7 (\pm 7.411 \cdot 10^3)_{stat}$
Max. Yield $N_{max,corr}$	$5.928 \cdot 10^7$	$2.266 \cdot 10^7$
Min. Yield $N_{min,corr}$	$5.535 \cdot 10^7$	$2.068 \cdot 10^7$
Δ $N_{+_{syst}}$	$(+0.168 \cdot 10^7)_{syst}$	$(+0.105 \cdot 10^7)_{syst}$
Δ $N_{-_{syst}}$	$(-0.225 \cdot 10^7)_{syst}$	$(-0.093 \cdot 10^7)_{syst}$

p_t-Y	π^-	π^+
Uncorr. Yield N_{uncorr}	$2.240 \cdot 10^7$	$8.323 \cdot 10^6$
Corr. Yield N_{corr}	$6.606 \cdot 10^7 (\pm 1.396 \cdot 10^4)_{stat}$	$2.054 \cdot 10^7 (\pm 7.120 \cdot 10^3)_{stat}$
Max. Yield $N_{max,corr}$	$6.818 \cdot 10^7$	$2.157 \cdot 10^7$
Min. Yield $N_{min,corr}$	$6.320 \cdot 10^7$	$1.965 \cdot 10^7$
Δ $N_{+_{syst}}$	$(+0.212 \cdot 10^7)_{syst}$	$(+0.105 \cdot 10^7)_{syst}$
Δ $N_{-_{syst}}$	$(-0.103 \cdot 10^7)_{syst}$	$(-0.089 \cdot 10^7)_{syst}$

TABLE 4.4: p-θ und p_t-Y uncorrected and corrected yields with statistical and systematical errors.

4.6 Determinition of Systematic Errors

The systematic errors have been obtained by the variation of the applied cuts and the resulting yields for the different sets.

The p-β-cut has been varied by 1σ, resulting in a wider and thighter cut of 4σ and 2σ respectively depicted in Fig. 4.19, where the red line depicts the original cut, while the white (4σ) and black (2σ) corresponds to the varied cuts.

As shown in Fig. 4.20 and 4.21, the cut on the primary vertex has also been varied. In Fig. 4.20 the black line illustrates the original cut of $R(x_{pv}, y_{pv}) \leq 20\,\text{mm}$, while the red line comlies with a selection range radius of $R(x_{pv}, y_{pv}) \leq 22\,\text{mm}$ and the pink line with $R(x_{pv}, y_{pv}) \leq 18\,\text{mm}$.

The cuts of the z-component of the reconstructed primary vertex have been changed to $-82\,\text{mm}$ to $7\,\text{mm}$ (blue) and $-78\,\text{mm}$ to $3\,\text{mm}$ (green) as depicted in Fig. 4.21.

With the varied cuts applied, the analysis leads to Fig. 4.22 and 4.23 for π^- and π^+ in p-θ and Fig. 4.24 and 4.25 for π^- and π^+ in p_t-Y. These yields have been obtained with integration of the used mass distributions and following efficiency and acceptance correction with correction matrices especially created for the varied cuts (see Appendix B).

The overall yields with statistical and systematical errors are shown in Tab. 4.4. The systematical errors were calculated using the difference between the corrected maximum and minimum yields with varied cuts to the corrected yield as in 4.4 and 4.5.

$$\Delta N_{+_{syst}} = N_{max,corr} - N_{corr} \tag{4.4}$$

$$\Delta N_{-_{syst}} = N_{min,corr} - N_{corr} \tag{4.5}$$

Those systematic errors are, as depicted in Tab. 4.4 of the same order as the yield values, but still small enough to enable distinct conclusions for the pion production.

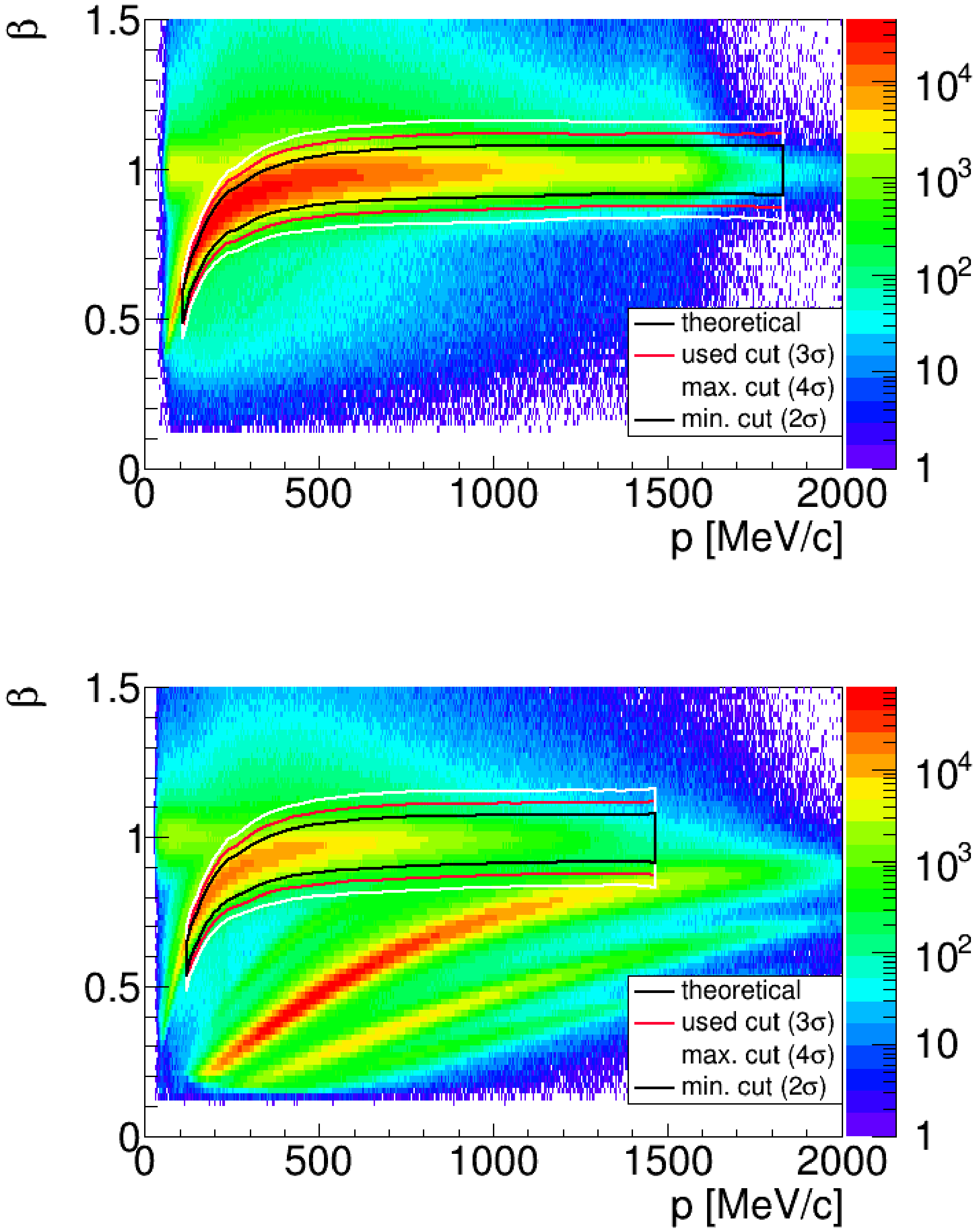

FIGURE 4.19: Particle velocity β as a function of the momentum for negative (top) and positive (bottom) charged particles. The red line indicates the applied 3σ cut for the pion selection, while the black and the white line show the varied cuts for the determination of the systematic errors.

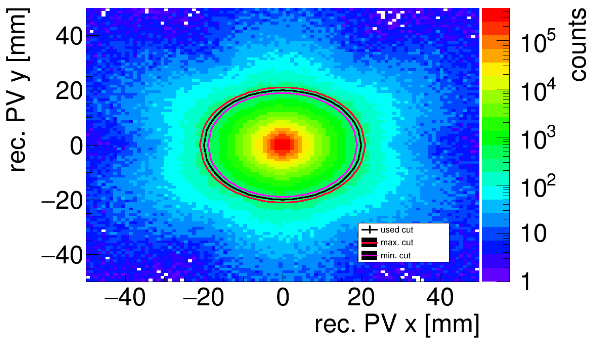

FIGURE 4.20: Reconstructed primary vertex in the x-y-plane. The selected region is indicated by the black circle, while the red and the pink line show the varied cuts for determination of the systematic errors.

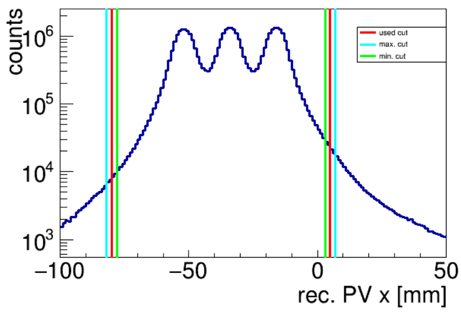

FIGURE 4.21: Reconstructed primary vertex in the direction of the incoming beam. The three peaks correspond to the target segments. A region from $-80\,\mathrm{mm}$ to $5\,\mathrm{mm}$ has been selected (black lines). For the upper and lower variation for the systematic errors the green line selects $-78\,\mathrm{mm}$ to $3\,\mathrm{mm}$ and the blue one $-82\,\mathrm{mm}$ to $7\,\mathrm{mm}$.

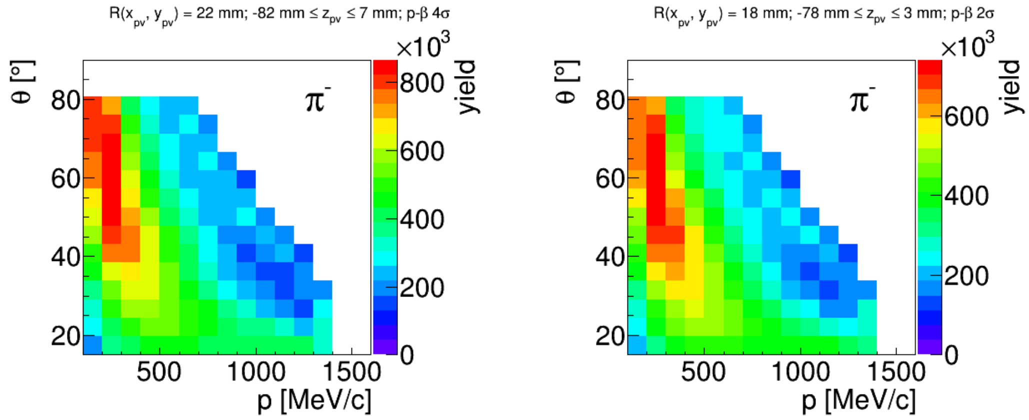

FIGURE 4.22: Maximum and minimum yield for p-θ and π^-. They have been achieved by integration over the mass distributions of p-θ for the varied cuts and following efficiency and acceptance correction.

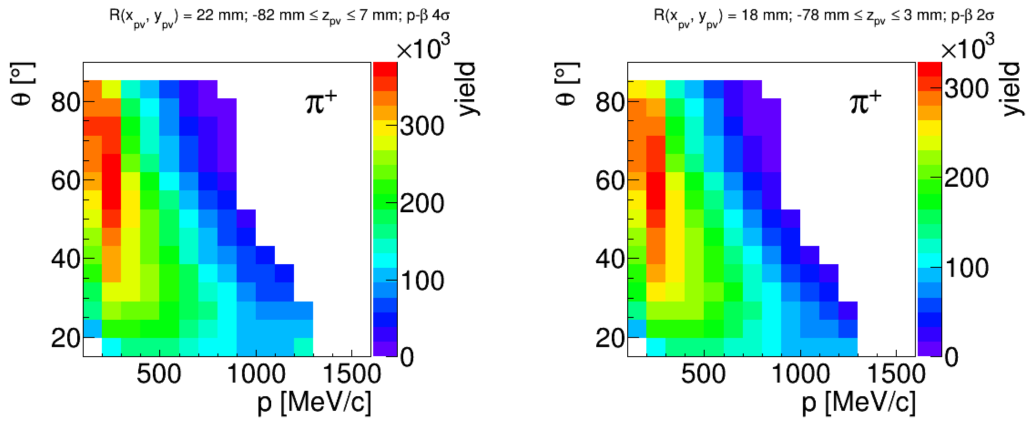

FIGURE 4.23: Maximum and minimum yield for p-θ and π^+. They have been achieved by integration over the mass distributions of p-θ for the varied cuts and following efficiency and acceptance correction.

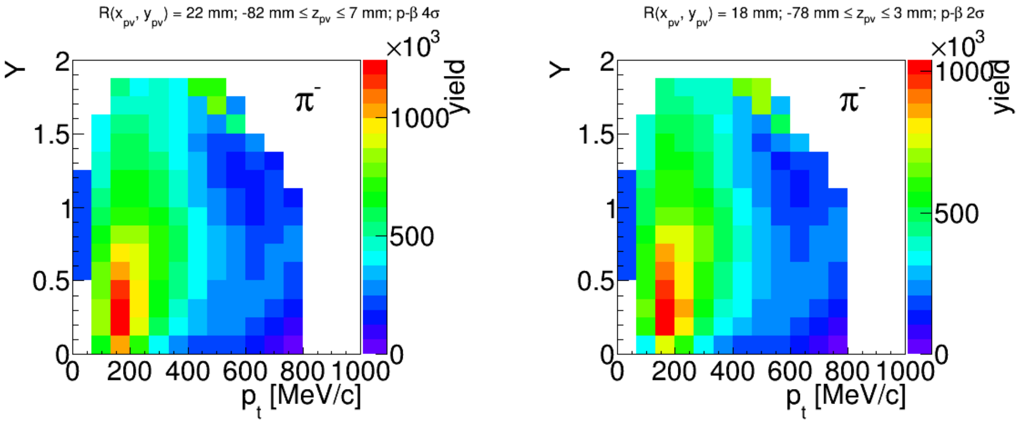

FIGURE 4.24: Maximum and minimum yield for p_t-Y and π^-. They have been achieved by integration over the mass distributions of p_t-Y for the varied cuts and following efficiency and acceptance correction.

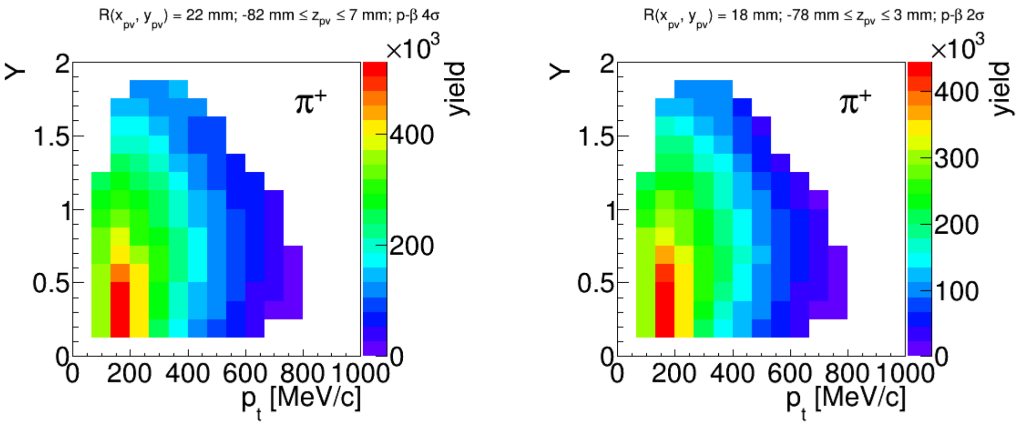

FIGURE 4.25: Maximum and minimum yield for p_t-Y and π^+. They have been achieved by integration over the mass distributions of p_t-Y for the varied cuts and following efficiency and acceptance correction.

5 Results and Discussion

5.1 Comparison of the p-θ yield-matrices to UrQMD and GiBUU

p-θ	π^-	π^+
Uncorr. Yield N_{uncorr}	$2.174 \cdot 10^7$	$8.502 \cdot 10^6$
Corr. Yield N_{corr}	$5.760 \cdot 10^7 (\pm 1.235 \cdot 10^4)_{stat}$	$2.161 \cdot 10^7 (\pm 7.411 \cdot 10^3)_{stat}$
Δ $N_{+_{syst}}$	$(+0.168 \cdot 10^7)_{syst}$	$(+0.105 \cdot 10^7)_{syst}$
Δ $N_{-_{syst}}$	$(-0.225 \cdot 10^7)_{syst}$	$(-0.093 \cdot 10^7)_{syst}$

TABLE 5.1: p-θ uncorrected and corrected yields with statistical and systematical errors.

In the following, the corrected p-$\boldsymbol{\theta}$ yield-matrices from the experimental data will be compared to the input yields of the transport models.
The overall number of pions can be seen in Tab. 5.1. Altogether, significantly more π^- than π_+ have been measured. This is originating from the elastic scattered beam pions and the enhanced number of π^- production channels in π^-A reactions in regard to the number of π^+ production channels [12]. Both transport models reproduce this behaviour.
The corrected yields for p-θ are shown in Fig. 5.1. For π^- (top) an increased region moving from momenta around 600 MeV / c and high θ to higher momenta and lower θ (red line) can be noted. In this region the elastic scattering of the beam particles is expected and therefore it can not be observed for π^+ (bottom).
When compared to UrQMD (Fig. 5.2) and GiBUU (Fig. 5.3), both transport models show the same behaviour as the experimental data, but with an enhanced elastic scattering peak (see red line), especially for UrQMD at high momenta.
The inelastic scattering peak for both π^- and π^+ at low momenta is better described by UrQMD than by GiBUU, as there the peak is moved to lower momenta and higher θ.
Altogether,the UrQMD model differs from the experimental data for high momenta, while GiBUU displays a better agreement with the experimental data in these ranges. For low momenta, the UrQMD model represents the inelastic scattering peak better than

GiBUU. Both models show the enhanced π^- production for π^-A reactions compared to the production of π^+.

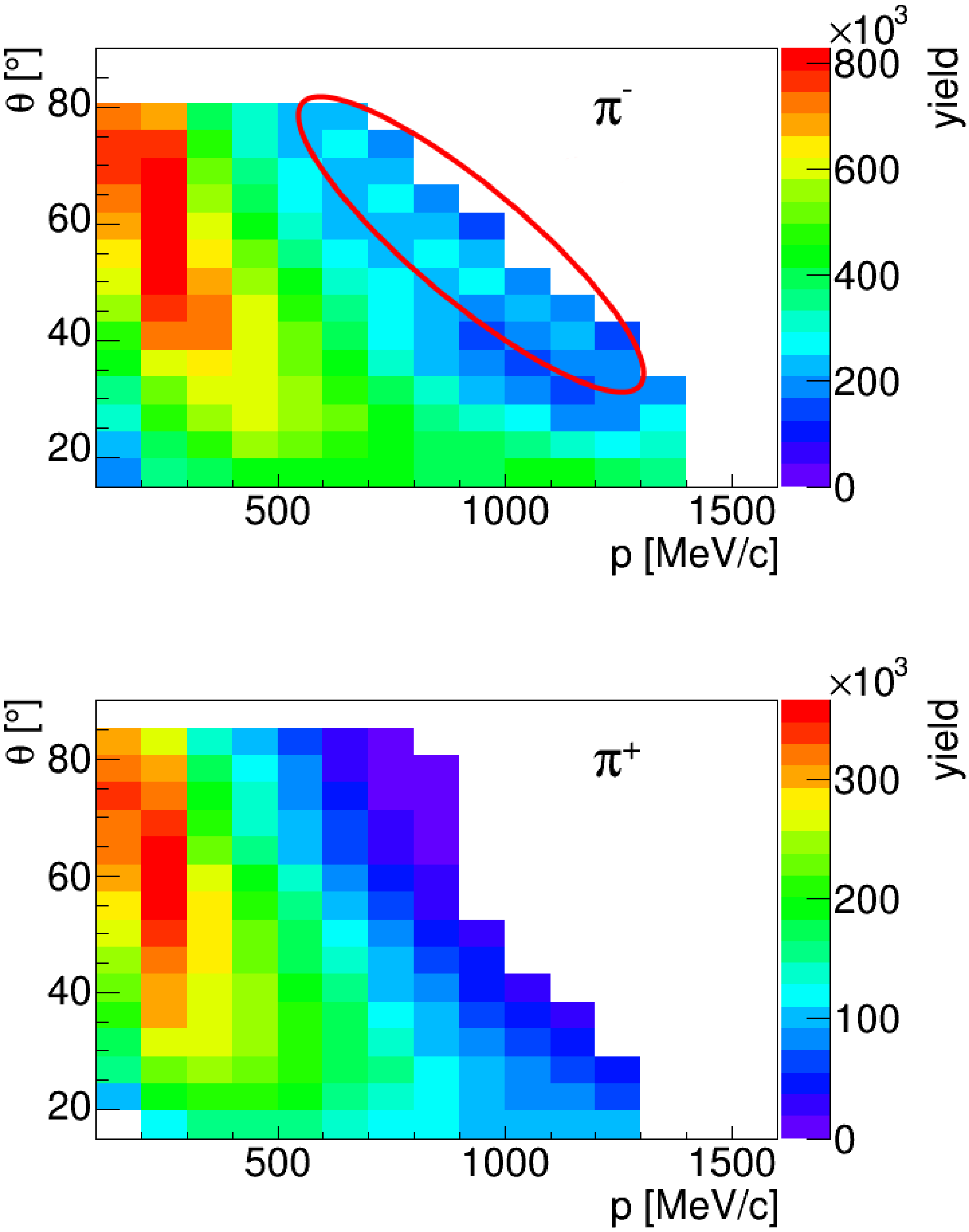

FIGURE 5.1: Corrected experimental p-θ yields, with the π^- spectrum in the top figure and the π^+ spectrum in the bottom one. The red line in the π^- figure marks the range where elastic scattering can possibly be seen.

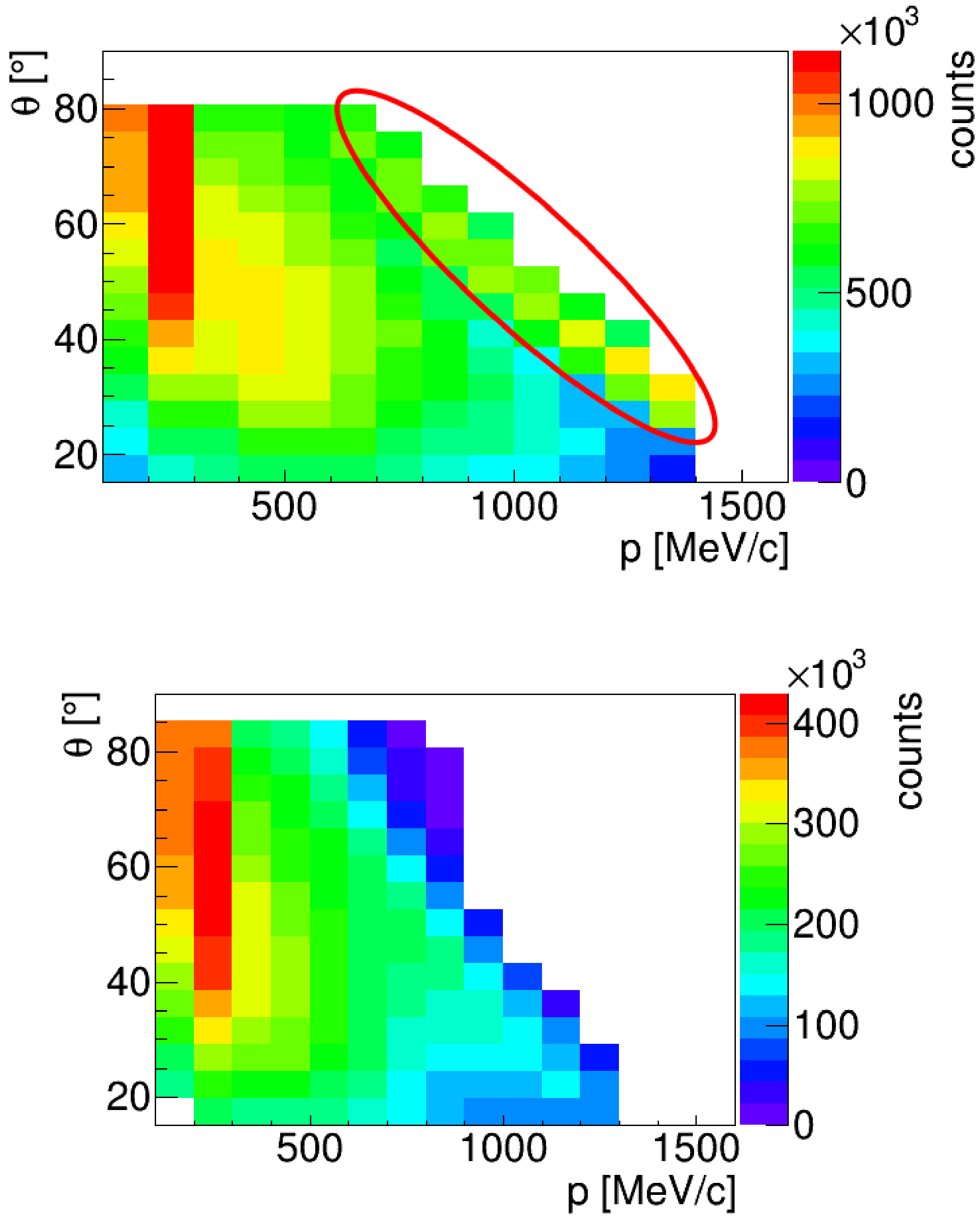

FIGURE 5.2: Corrected p-θ yields for UrQMD, with the π^- spectrum in the top figure and the π^+ spectrum in the bottom one. The red line in the π^- figure marks the range where elastic scattering can possibly be seen.

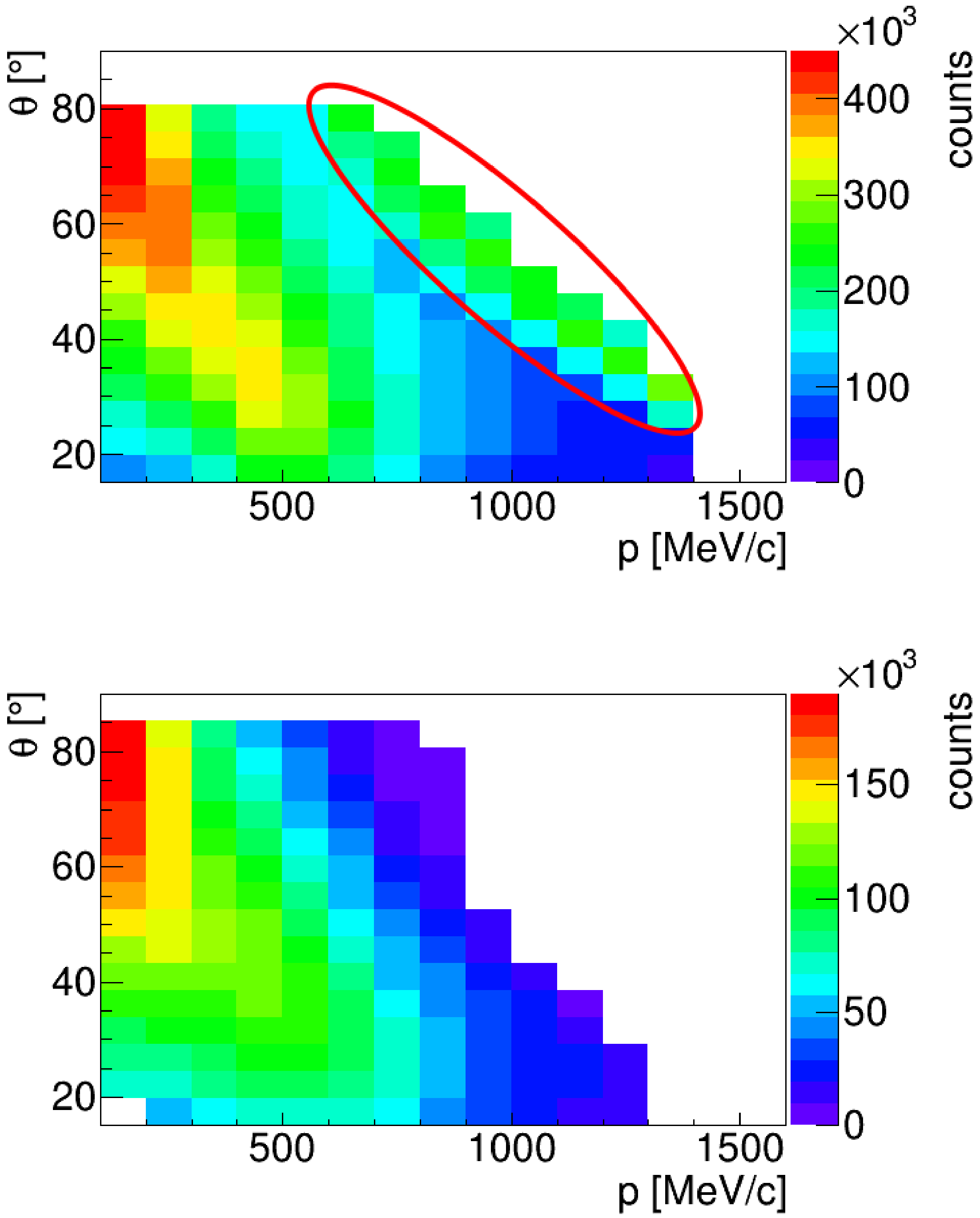

FIGURE 5.3: Corrected p-θ yields for GiBUU, with the π^- spectrum in the top figure and the π^+ spectrum in the bottom one. The red line in the π^- figure marks the range where elastic scattering can possibly be seen.

5.2 Comparison of the p_t-Y yield-matrices to UrQMD and GiBUU

p_t-Y	π^-	π^+
Uncorr. Yield N_{uncorr}	$2.240 \cdot 10^7$	$8.323 \cdot 10^6$
Corr. Yield N_{corr}	$6.606 \cdot 10^7 (\pm 1.396 \cdot 10^4)_{stat}$	$2.054 \cdot 10^7 (\pm 7.120 \cdot 10^3)_{stat}$
$\Delta\ N_{+_{syst}}$	$(+0.212 \cdot 10^7)_{syst}$	$(+0.105 \cdot 10^7)_{syst}$
$\Delta\ N_{-_{syst}}$	$(-0.103 \cdot 10^7)_{syst}$	$(-0.089 \cdot 10^7)_{syst}$

TABLE 5.2: p_t-Y uncorrected and corrected yields with statistical and systematical errors.

Similar to the p-θ yields presented in the section above, the p_t-Y distributions include significantly more π^- than π^+ as presented in Tab. 5.2. This is reasoned by the enhanced number of π^- production channels for π^-A reactions [12] and the elastic scattered beam pions as stated before.
The experimental yields for the p_t-Y distributions of π^- (top) and π^+ (bottom) are depicted in Fig. 5.4. The inelastic scattering peak is located at low transverse momenta and rapidities, while for the negative pions again an enhanced region at high p_t can be observed (red line). This region could possibly be reasoned by the elastic scattering of the beam pions with the target nuclei.
When compared to the transport model GiBUU, a good conformity for π^+ can be noted, while UrQMD has an in comparison enhanced region for higher transverse momenta.
For π^- both models display the peak in the red framed region, which is possible to arise from elastic scattering. However, similar to the p-θ distributions, this peak is in comparison to the inelastic scattering larger for both models, particularly for UrQMD.
Summing up, the transport models describe the enhanced production of π^- well, but especially UrQMD differs for high transverse momenta from the experimental distribution, while GiBUU shows a better conformity.

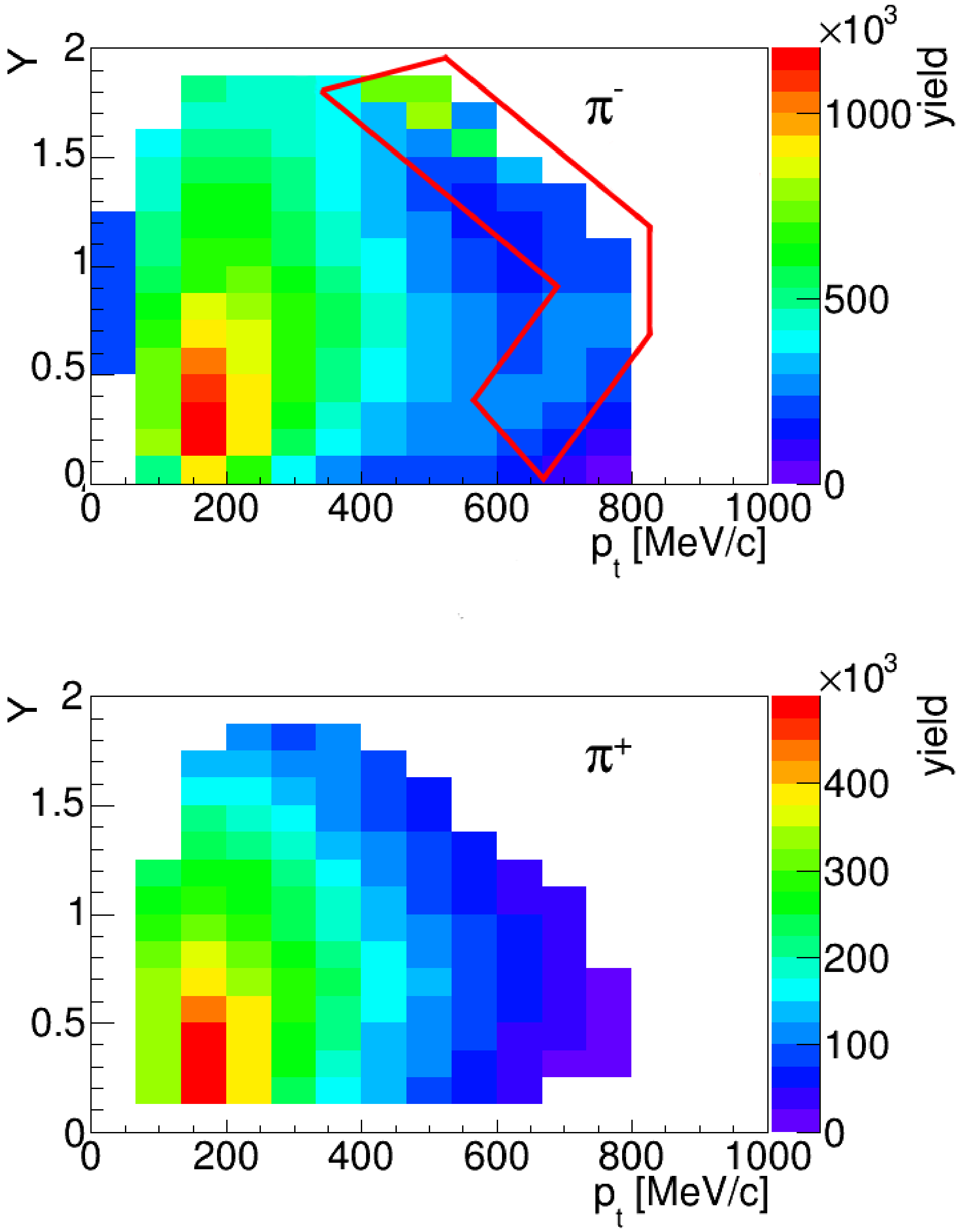

FIGURE 5.4: Corrected experimental p_t-Y yields, with the π^- spectrum in the top figure and the π^+ spectrum in the bottom one. The red line in the π^- figure marks the range where elastic scattering can possibly be seen.

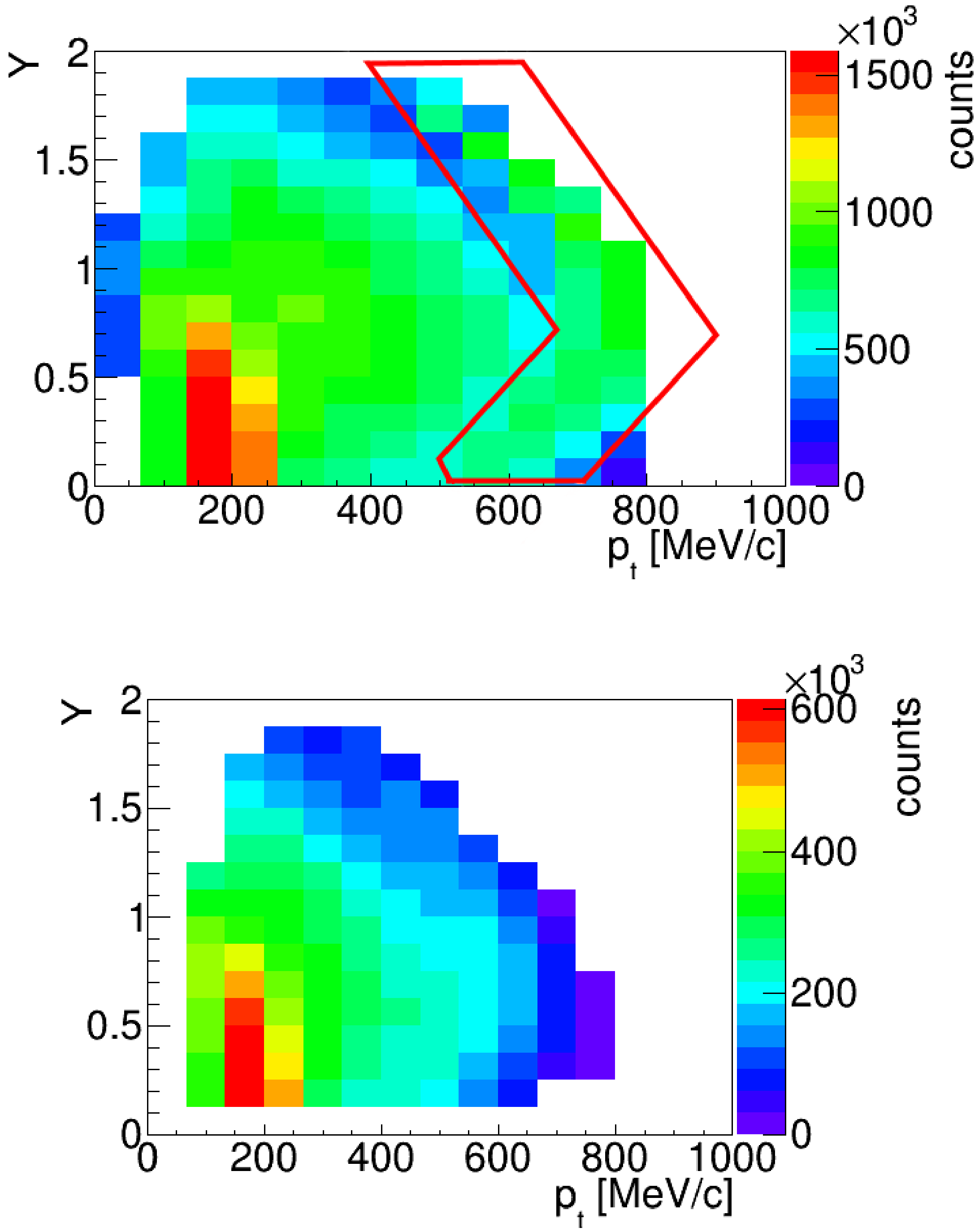

FIGURE 5.5: Corrected p_t-Y yields for UrQMD, with the π^- spectrum in the top figure and the π^+ spectrum in the bottom one. The red line in the π^- figure marks the range where elastic scattering can possibly be seen.

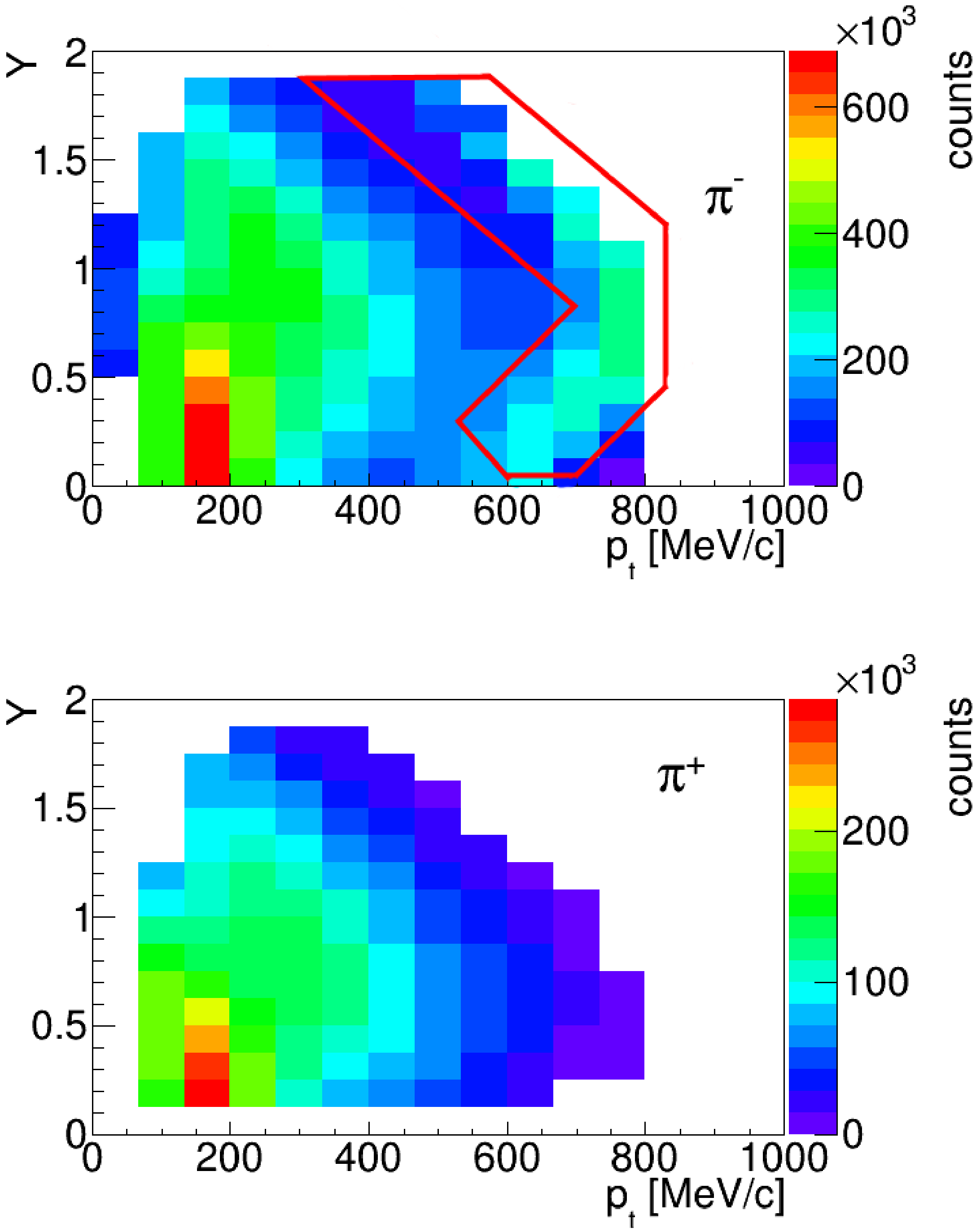

FIGURE 5.6: Corrected p_t-Y yields for GiBUU, with the π^- spectrum in the top figure and the π^+ spectrum in the bottom one. The red line in the π^- figure marks the range where elastic scattering can possibly be seen.

5.3 Comparison of the dN/dp_tdY and dN/dY distributions to UrQMD and GiBUU

To monitor the behaviour of the yield for different p_t and Y, the two-dimensional histograms from the section above (see Fig. 5.4) have been projected to their x-axis, showing the dN/dp_tdY spectra for varying rapidity ranges. With integration and extrapolation of those plots, a dN/dY distribution can be achieved.
The dN/dp_tdY distributions for π^+ are shown in Fig. 5.7. The transport models have been scaled to fit to the size of the experimental data and compare the distributions. The experimental data (black) and the GiBUU transport model (green) show good resemblance for most of the bins. In the rapidity region above 1.5, GiBUU is starting to differ from the experimental data points. This could also be noted for the matrices in the section above (see Fig. 5.6).
On the other hand, UrQMD fits to the experimental data for lower p_t, but forms a peak at higher transverse momenta, which is not in agreement with the experimental data.

The dark grey line in Fig. 5.7 indicates the Boltzmann extrapolation which was conducted to the experimental data. The Boltzmann function 5.1 was chosen since the shape of the data is in good resemblance with it. With the inserted pion mass, the shape of the curve depends only on the two parameters p_1 and p_2.

$$y = p_1 x \cdot \sqrt{x^2 + m_\pi^2} \cdot \mathrm{e}^{-\frac{\sqrt{x^2+m_\pi^2}}{p_2}} \tag{5.1}$$

To receive the integral over the whole p_t range, the fit function was applied to determine the integral for ranges where no data points are available. The sum of the integral over the data points and the extrapolation from the fit lead to the $1/\Delta y$ dN/dY plot depicted in Fig. 5.8. The factor $1/\Delta y$ is reasoned by the normalisation of the plot on the bin width Δy.
The UrQMD (red) and GiBUU (green) rapidity spectra have been scaled so they can be compared to the shape of the experimental data. In general the courses resemble each other, but for higher rapidities, the Boltzmann extrapolation of the experimental data declines slower than the two simulations. This could be reasoned by the low number of available points in the dN/dp_tdY distributions, where the Boltzmann fit had to be used for wide ranges of the spectrum.

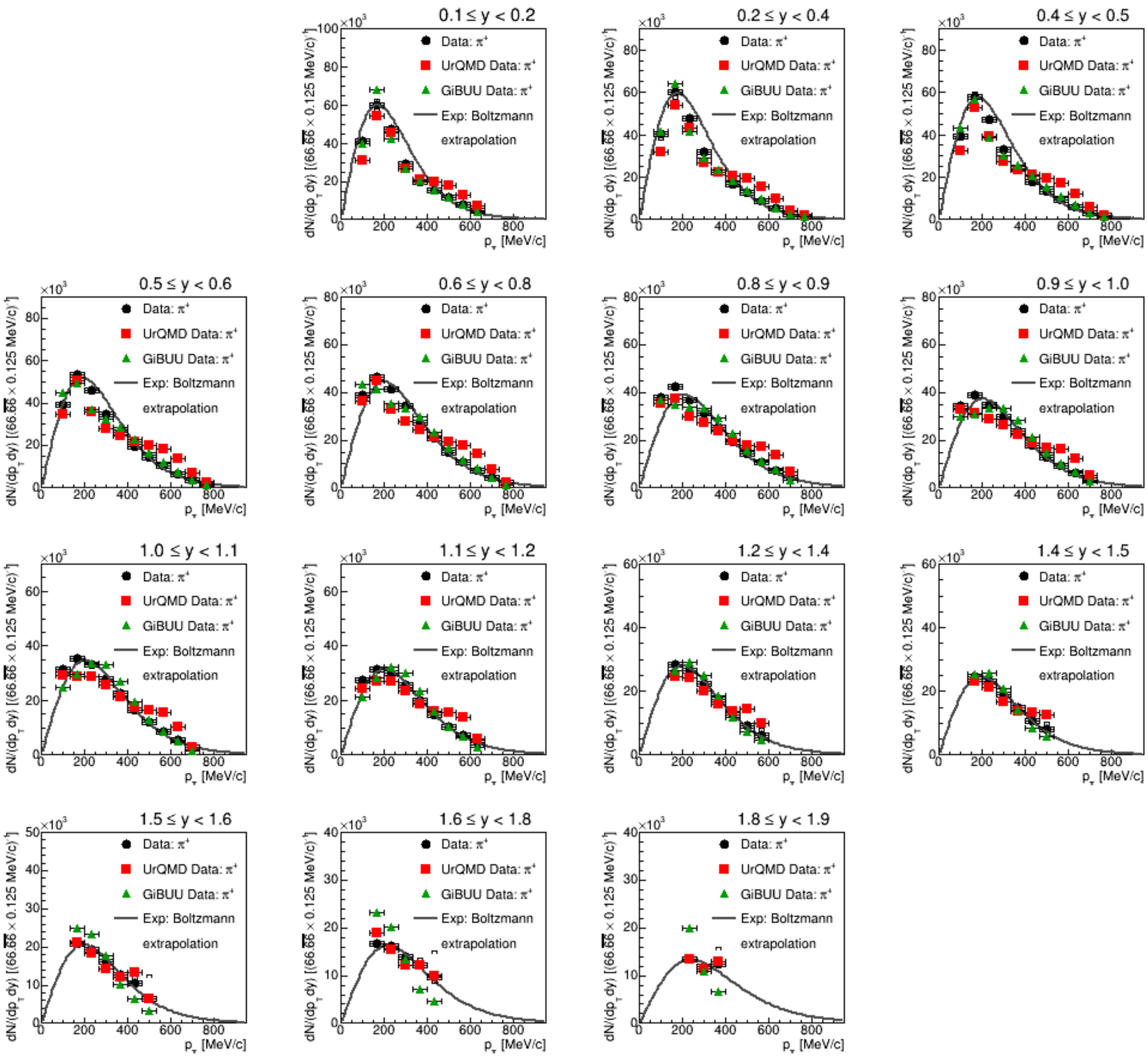

FIGURE 5.7: dN/dp_tdY distributions for π^+ and different rapidity ranges. The experimental data is plotted in black, while UrQMD is shown in red and GiBUU in green. The dark grey function resembles the Boltzmann extrapolation executed on the experimental data.

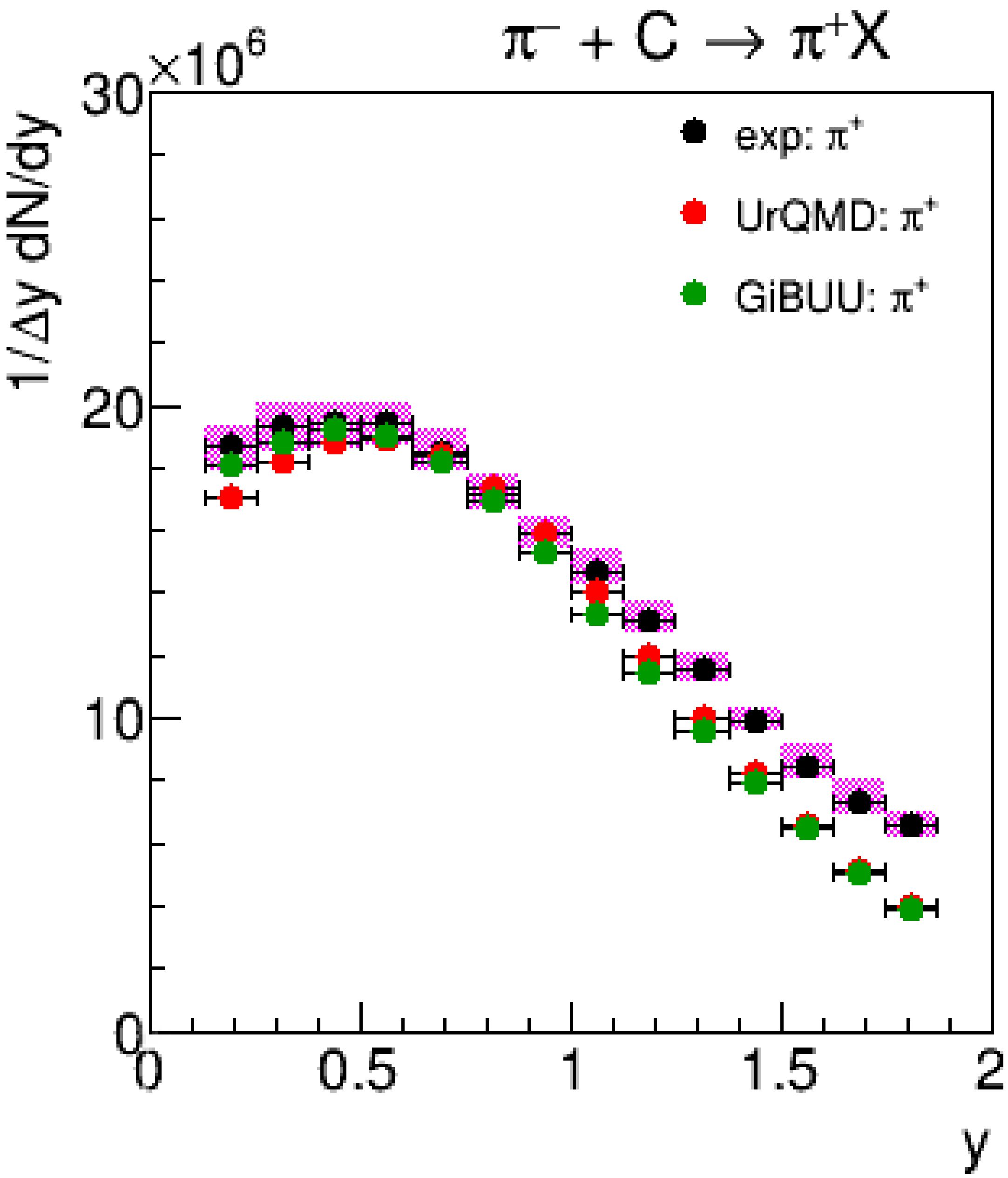

FIGURE 5.8: $1/\Delta y$ dN/dY distribution for π^+ normalized on the bin width. The experimental data is plotted in black, with the systematic errors drawn in pink. UrQMD is symbolized by red markers, while GiBUU is painted in green.

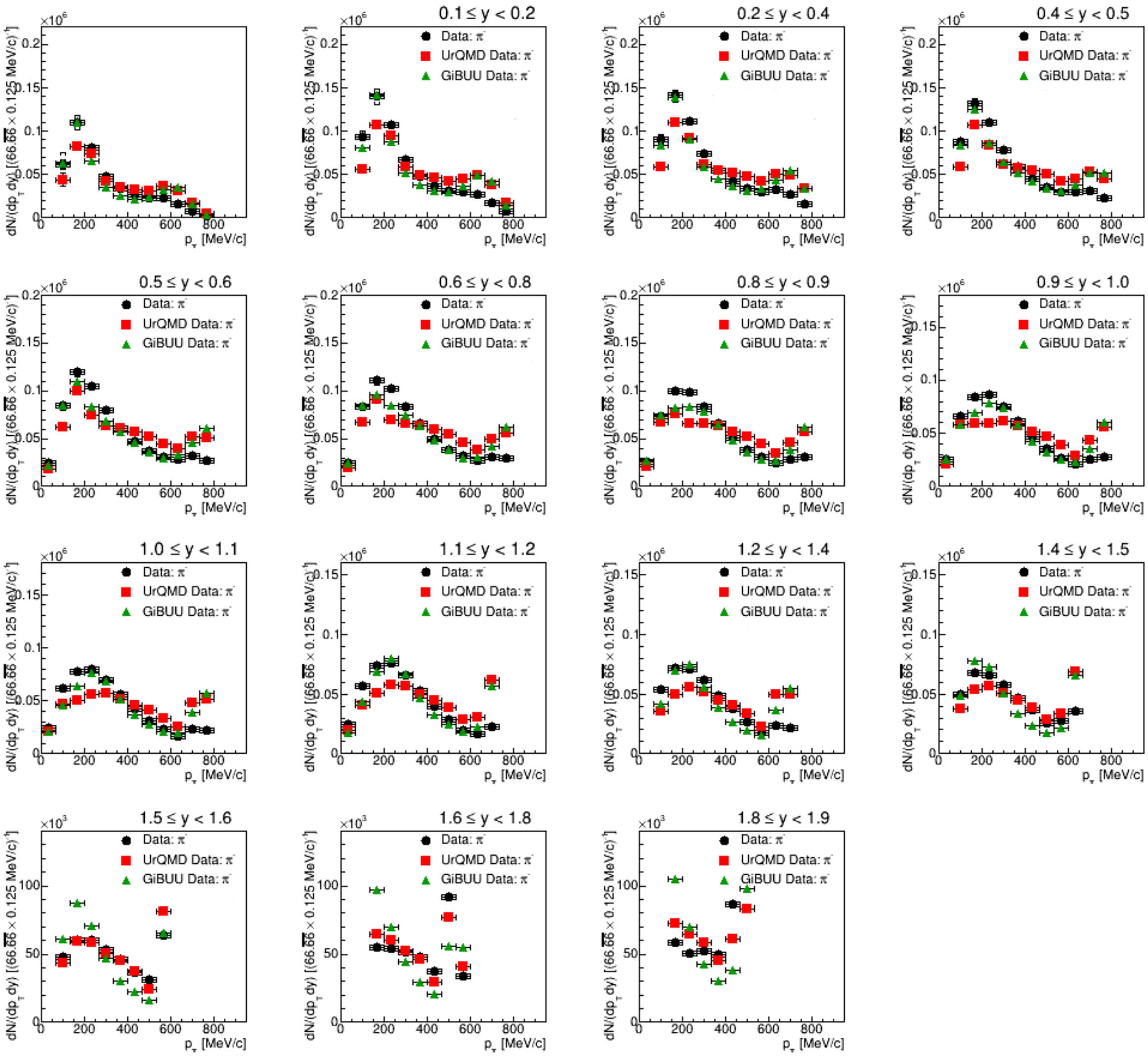

FIGURE 5.9: dN/dp$_t$dY distributions for π^- and different rapidity ranges. The experimental data is plotted in black, while UrQMD is shown in red and GiBUU in green.

The dN/dp$_t$dY distributions for π^- are depicted in Fig. 5.9. As the p$_t$-Y matrices included a peak, which could possibly be reasoned by elastic scattering, the spectra in Fig. 5.9 have a second peak at high transverse momenta. While GiBUU resembles the experimental curve well, except for high rapidities as noted before, UrQMD differs from the experimental data. The peak of UrQMD for high transverse momenta is more distinct than the other ones.
To extrapolate these distributions, the π^+ (blue) had been scaled to the same amplitude as the π^- (black) as illustrated in Fig. 5.10. The structure of the inelastic scattering peak for both π^+ and π^- is equivalent, therefore the Boltzmann fit (blue line) had been conducted to the scaled positive pions to extract the π^- inelastic production.

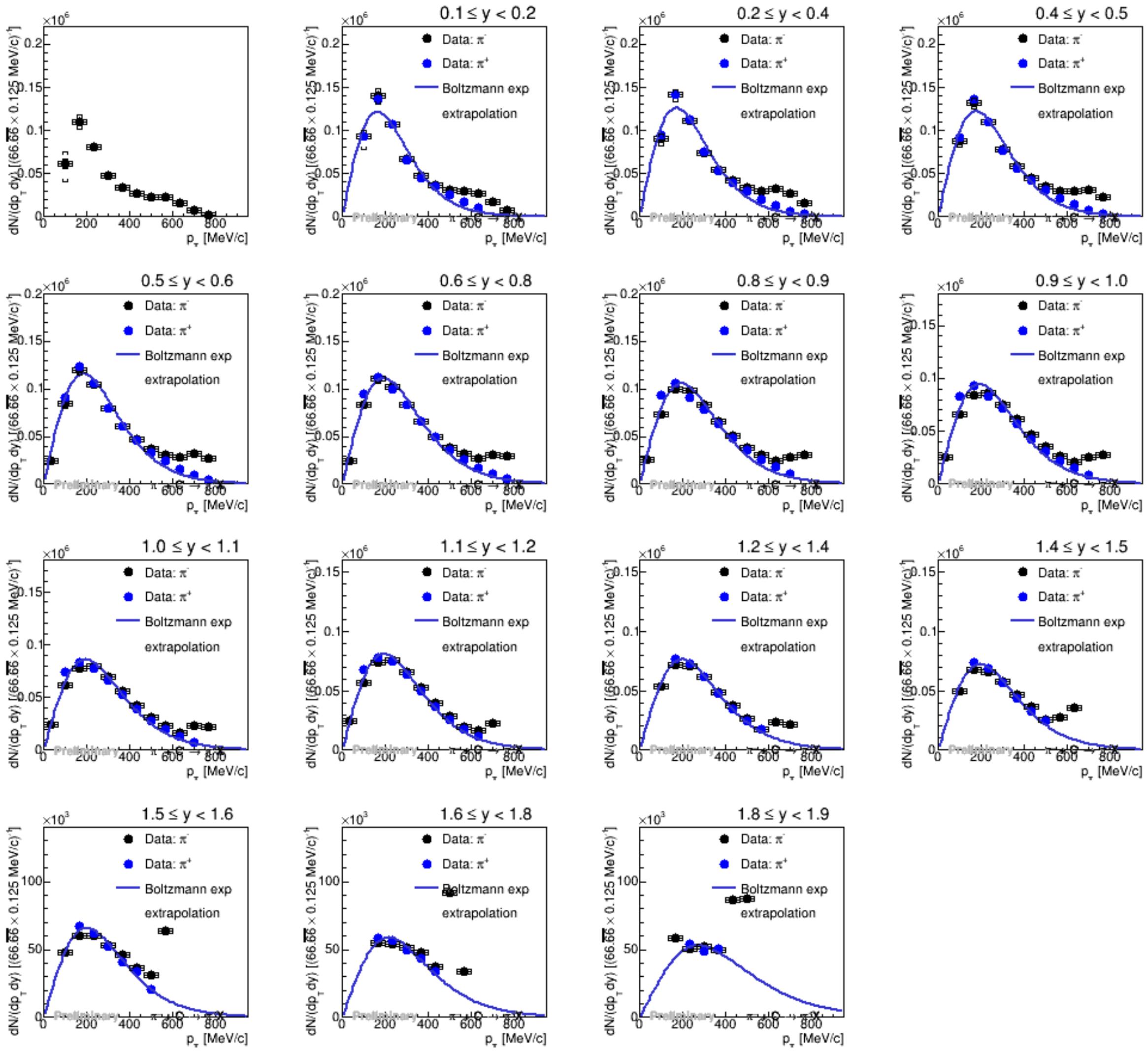

FIGURE 5.10: dN/dp$_t$dY distributions and different rapidity ranges. The π^+ (blue) distributions have been scaled to fit to the size of the pi^- (black). The blue line depicts the Boltzmann extrapolation for the inelastic scattering peak of π^-.

To achieve the values for the $1/\Delta y$ dN/dY distribution plotted in Fig. 5.11, the Boltzmann fit integral for had not only been added for regions where no data was available, but also for the second peak. The integral of the dN/dp$_t$dY spectra was only conducted for the inelastic peak to get the pion production.
The experimental plot (black) in Fig. 5.11 is result of this Boltzmann extrapolation. Both GiBUU (green) and UrQMD (red) were scaled to the same size and behave similar to the experimental data. Especially for high rapidities, the plots are in good agreement with each other. The relatively high systematic errors and discrepancies at low rapidities could be reasoned by the Boltzmann extrapolation for very low transverse momenta (ap-

proximately 0 MeV / c to maximum 100 MeV / c). In these ranges, it is possible for the Boltzmann function not to fit perfectly to the shape of the actual distribution, leading to a too large integral.

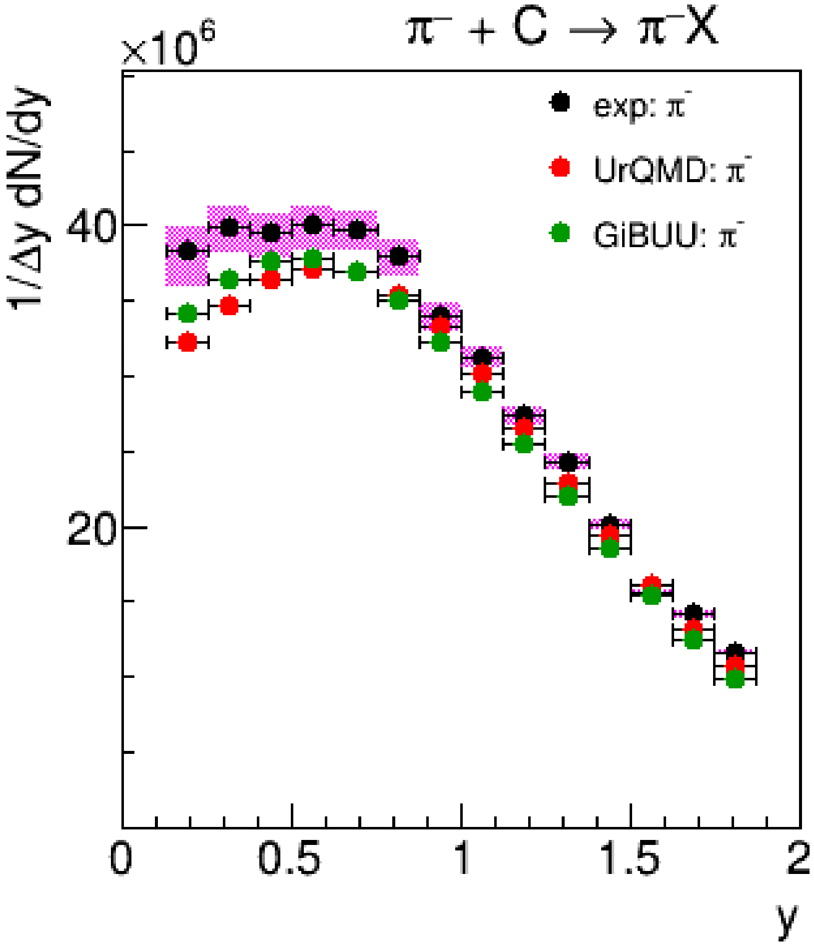

FIGURE 5.11: $1/\Delta y$ dN/dY distribution for π^- normalised on the bin width. The experimental data is plotted in black, with the systematic errors drawn in pink. UrQMD is symbolised by red markers, while GiBUU is painted in green.

To sum up, the GiBUU transport model describes the data in transverse momentum dependent distributions better than UrQMD except for high rapidities. Both transport models lead to equivalent dN/dY spectra, which fit the experimental data well.

6 Conclusion

Summing up, p-θ and p_t-Y spectra for π^- and π^+ originated by π^-C reactions at a beam momentum of 1.7 GeV / c were created. For p_t-Y, dN/dp_tdY distributions were generated and used to extrapolate the dN/dY spectra for inelastic production of both particles. Additionally, these results have been compared to the UrQMD and GiBUU transport models.
For π^- a potential elastic scattering peak has been observed and excluded from the final dN/dY spectrum. The overall π^- production was higher than the one for π^+, reasoned by the higher number of available production channels.
The comparison to the transport models led to a better agreement of GiBUU with the experimental data, since UrQMD showed additional effects leading to peaks at high p and p_t. On the other hand, it described the experimental distribution at high rapidities better than GiBUU.
With the yields achieved in this thesis, charged pion production cross sections for π^-C reactions at a beam momentum of 1.7 GeV / c could be calculated in the future to achieve a better understanding of the pion-nucleus interaction and set new points in the HARP data mentioned in the introduction.

A p-β-Spectra for UrQMD and GiBUU

As the cuts und the p-β spectrum have been generated for experimental data and the transport models individually, the figures A.1 and A.2 show the p-β distribution for UrQMD and GiBUU. Negative particles are in both cases depicted in the top figure, while positive particles are shown in the bottom one.

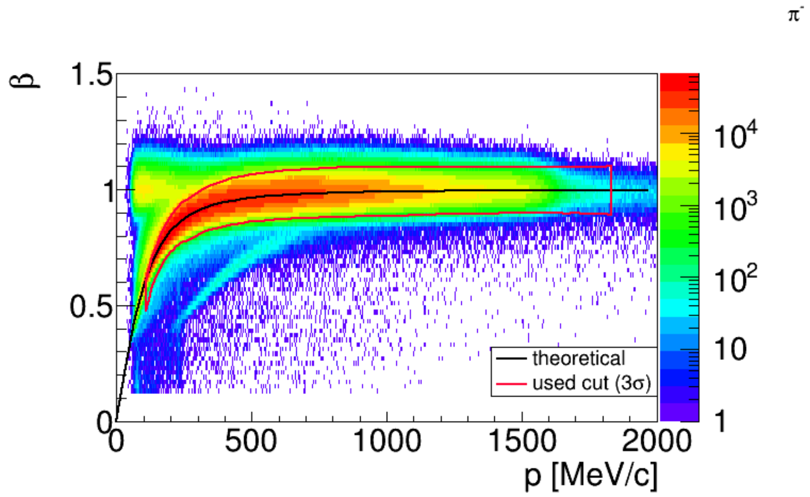

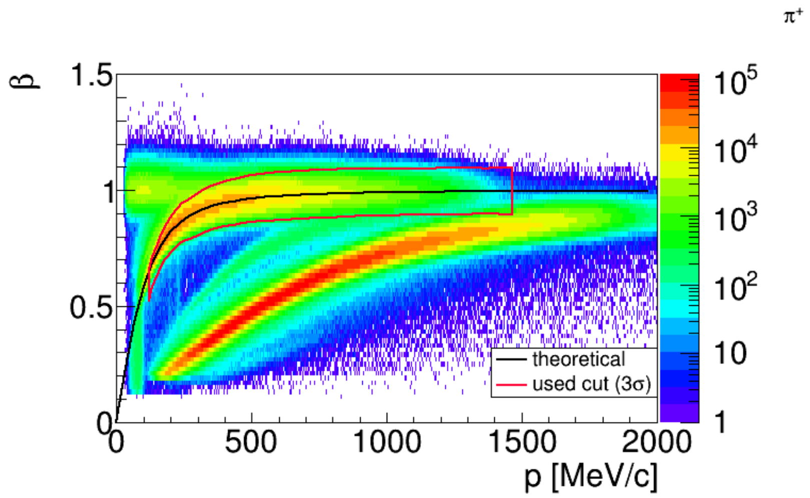

FIGURE A.1: p-β spectrum for UrQMD with theoretical curve (black) and applied cut (red). Negative particles are shown in the upper, positive ones in the bottom figure.

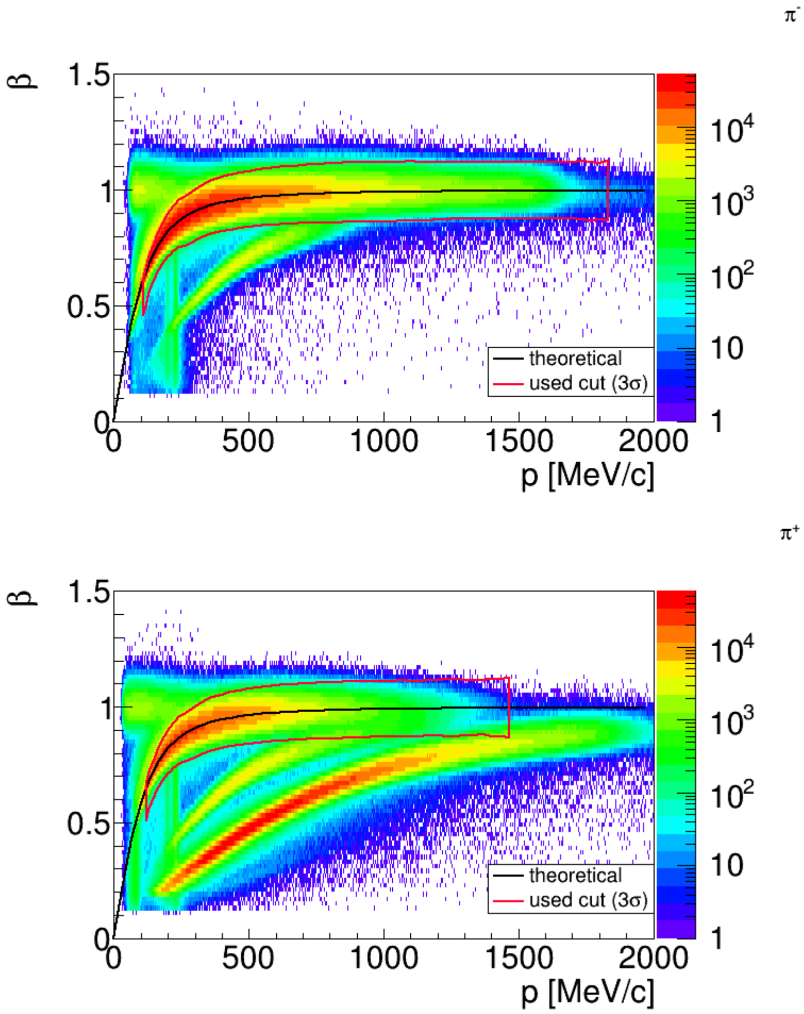

FIGURE A.2: p-β spectrum for GiBUU with theoretical curve (black) and applied cut (red). Negative particles are shown in the upper, positive ones in the bottom figure.

B p-θ and p_t-Y-Yields for the Determination of the Systematic Errors

For the systematic error determination new efficiency and acceptance correction matrices have to be generated, as the correction varies with the size of the cuts. Those matrices are shown in Fig. B.1, B.2, B.3 and B.4.

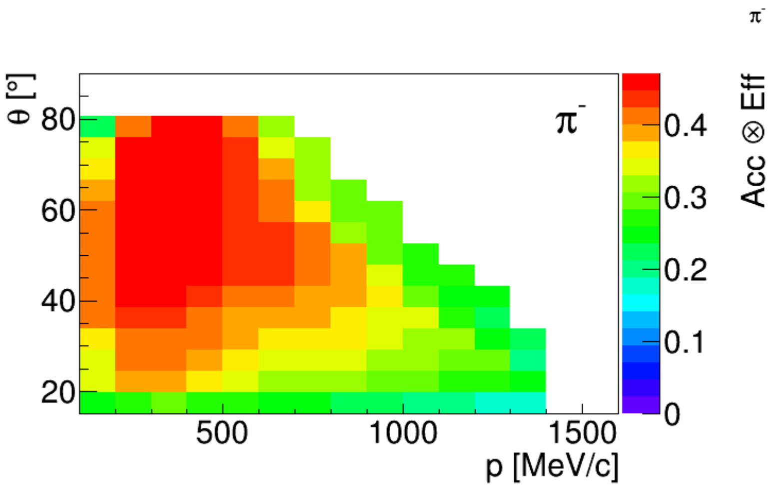

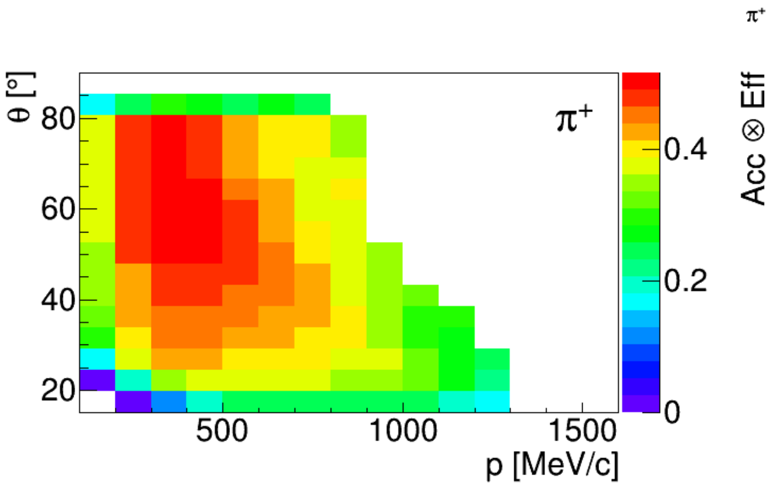

FIGURE B.1: Efficiency and acceptance correction matrices for p-θ for π^- (top) and π^+ (bottom) for 4σ p-β, $-82\,\mathrm{mm} \leq z_{pv} \leq 7\,\mathrm{mm}$ and $R(x_{pv}, y_{pv}) \leq 22\,\mathrm{mm}$ cuts for the systematic error determination.

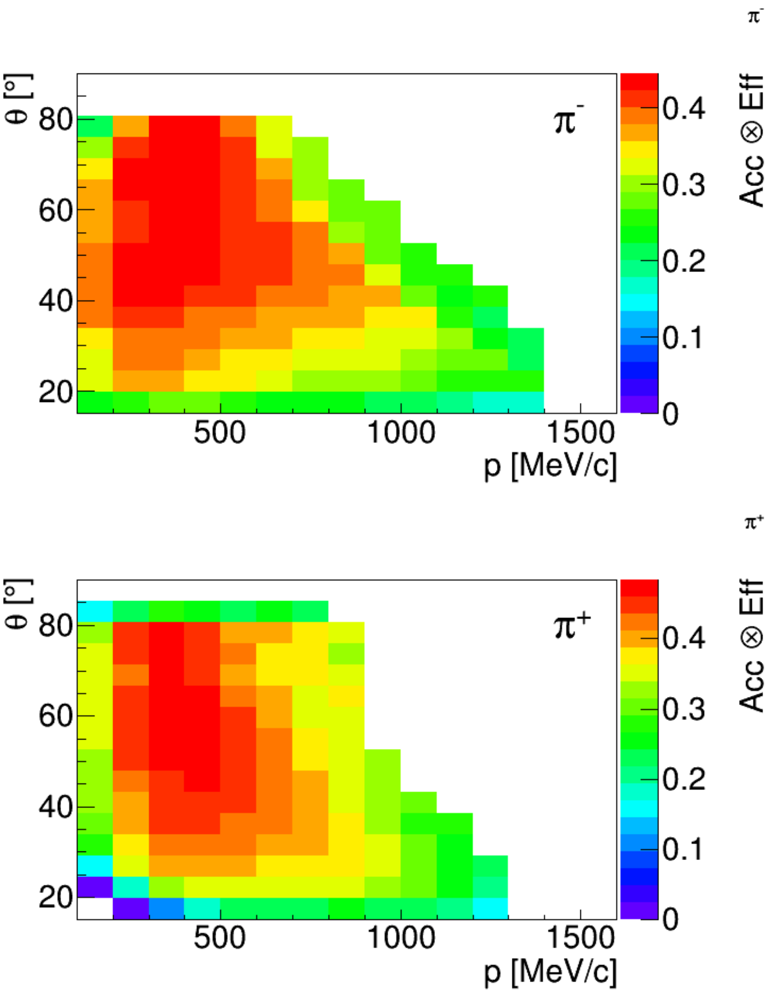

FIGURE B.2: Efficiency and acceptance correction matrices for p-θ for π^- (top) and π^+ (bottom) for 2σ p-β, $-78\,\mathrm{mm} \leq z_{pv} \leq 3\,\mathrm{mm}$ and $R(x_{pv}, y_{pv}) \leq 18\,\mathrm{mm}$ cuts for the systematic error determination.

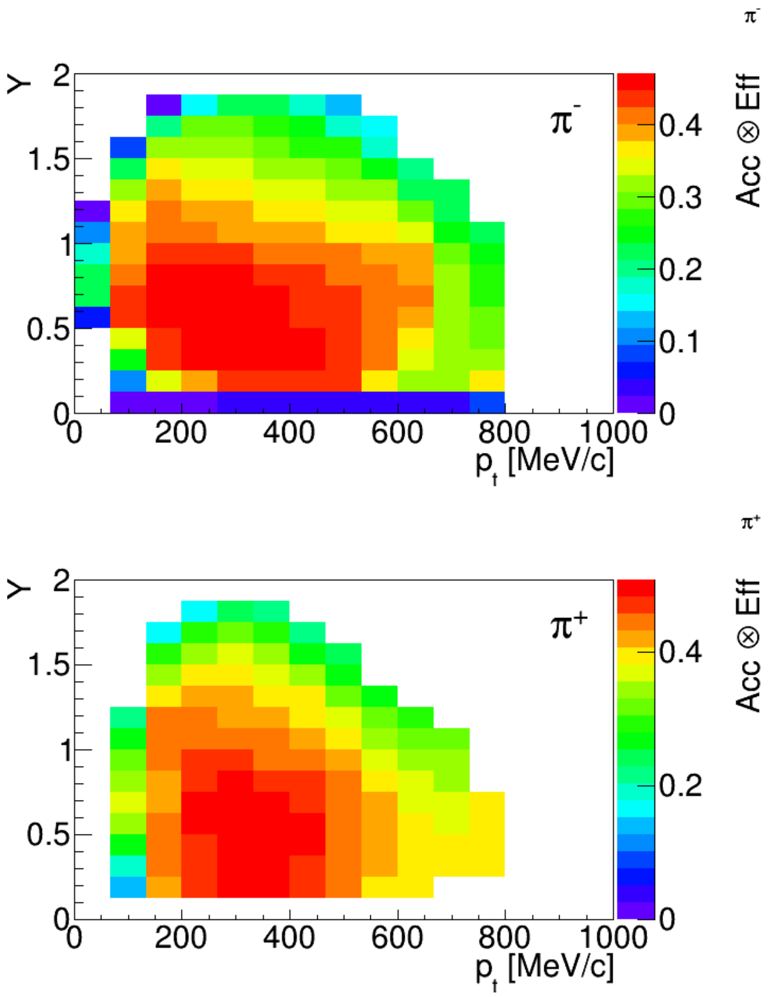

FIGURE B.3: Efficiency and acceptance correction matrices for p$_t$-Y for π^- (top) and π^+ (bottom) for 4σ p-β, $-82\,\mathrm{mm} \leq z_{pv} \leq 7\,\mathrm{mm}$ and $R(x_{pv}, y_{pv}) \leq 22\,\mathrm{mm}$ cuts for the systematic error determination.

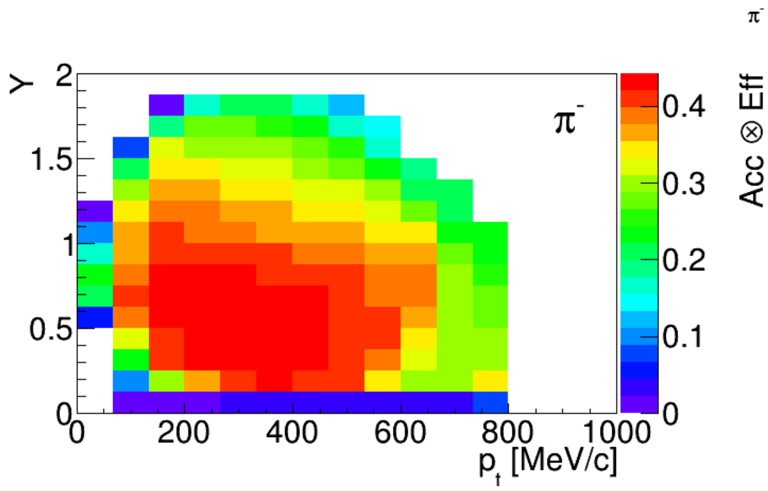

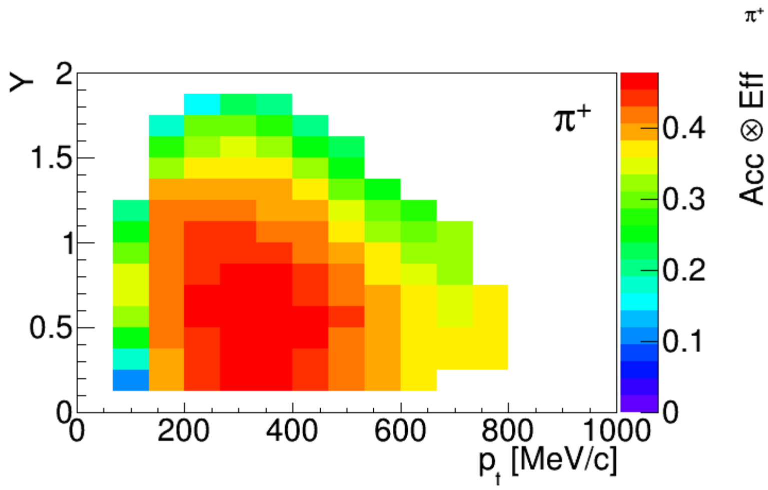

FIGURE B.4: Efficiency and acceptance correction matrices for p_t-Y for π^- (top) and π^+ (bottom) for 2σ p-β, $-78\,\mathrm{mm} \leq z_{pv} \leq 3\,\mathrm{mm}$ and $R(x_{pv}, y_{pv}) \leq 18\,\mathrm{mm}$ cuts for the systematic error determination.

Bibliography

[1] Christoph Scholz Frank Zetsche Werner Rodejohann Bogdan Povh, Klaus Rith. *Particles and Nuclei - An Introduction to the Physical Concepts*. Springer, 7th edition, 2014. page 298.

[2] The HADES collaboration. The HADES website. https://hades-new.gsi.de.

[3] The HADES collaboration. The high-acceptance dielectron spectrometer HADES. *Eur. Phys. J. A 41, 243277*, 2009.

[4] The UrQMD collaboration. The UrQMD model. https://urqmd.org/.

[5] M. L. Benabderrahmane et al. Measurement of the In-Medium K^0 Inclusive Cross Section in π^--Induced Reactions at 1.15 GeV / c. *Phys. Rev. Lett. 102, 182501*, 2009.

[6] M. Apollonio et al. (HARP Collaboration). Large angle production of charged pions with incident pion beams on nuclear targets. *Phys. Rev. C80, 065207*, 2009.

[7] The GiBUU group. The GiBUU project. https://gibuu.hepforge.org/trac/wiki.

[8] The Particle Data Group. The Particle Data Group Website. http://pdg.lbl.gov.

[9] L. Fabbietti I. Frhlich T. Hennino W. Knig H. Kuc R. Lalik P. Louis L. Maier R. Mnzer J. Pietraszko B. Ramstein P. Salabura T. Schmitt E. Schwab J. Siebenson M. Traxler J. Biernat, E. Epple and J. Wirth. A Secondary Pion Beam for the HADES Experiment. 2013.

[10] T. Kunz. *Private communications.*

[11] M. Bleicher, E. Zabrodin, C. Spieles, S.A. Bass, C. Ernst, S. Soff, H. Weber, H. Stöcker and W. Greiner. Relativistic hadronhadron collisions in the ultra-relativistic quantum molecular dynamics model. *J. Phys. G25 (1999) 18591896*, 1999.

[12] Springer International Publishing. Landolt-Brnstein Database. http://materials.springer.com/.

[13] Christian Wendisch. Hyperon-Produktion und -Polarisation in der Reaktion p (3,5 GeV) + Nb mit HADES. http://nbn-resolving.de/urn:nbn:de:bsz:14-qucosa-158395.

[14] J. Wirth. *Private communications.*

Acknowledgement

I want to thank Prof. Dr. Laura Fabbietti, who gave me the opportunity to work in her group and learn much about data analysis and particle physics. I am honoured that was able to write my bachelor thesis under her supervision.
Furthermore, lots of gratitude to both of my supervisors, Joana Wirth and Steffen Maurus, for their patience and support, especially in the last two weeks. You were great!
Additionally, many thanks to Tobias Kunz, who proofread big parts of this thesis and helped a lot with the corrections.
At last, thanks to the whole group for the sympathic working atmosphere!